

# Intermolecular potential energy surface of the proton-bound $\text{H}_2\text{O}^+$ –He dimer: *Ab initio* calculations and IR spectra of the O–H stretch vibrations

Doris Roth, Otto Dopfer\* and John P. Maier

Institute for Physical Chemistry, University of Basel, Klingelbergstrasse 80, CH-4056 Basel, Switzerland. E-mail: otto.dopfer@unibas.ch

Received 13th February 2001, Accepted 3rd April 2001

First published as an Advance Article on the web 24th May 2001

Rotationally resolved infrared photodissociation spectra of the O–H stretch fundamentals ( $\nu_1$  and  $\nu_3$ ) of the  $\text{H}_2\text{O}^+$ –He open shell ionic complex have been recorded in the doublet electronic ground state. The analysis of the complexation-induced frequency shifts ( $\Delta\nu_1 = -15 \text{ cm}^{-1}$ ,  $\Delta\nu_3 = -5.1 \text{ cm}^{-1}$ ) and the rotational structure is consistent with a planar, translinear proton-bound H–O–H–He equilibrium geometry. The derived intermolecular H–He separation and O–H–He bond angle are  $R_0 = 1.756(4) \text{ \AA}$  and  $\phi_0 = 175(5)^\circ$  in the ground vibrational state. The experimental results are in good agreement with the *ab initio* calculations performed at the unrestricted MP2 level using a basis set of aug-cc-pVTZ quality. The global minimum on the calculated potential energy surface features a slightly translinear proton-bound equilibrium geometry, with an intermolecular separation of  $R_e = 1.6990 \text{ \AA}$ , a bond angle of  $\phi_e = 173.2^\circ$ , dissociation energies of  $D_e = 425.9 \text{ cm}^{-1}$  and  $D_0 = 158.6 \text{ cm}^{-1}$ , and frequency shifts of  $\Delta\nu_1 = -34.4 \text{ cm}^{-1}$  and  $\Delta\nu_3 = -11.6 \text{ cm}^{-1}$ . Tunneling splittings in the perpendicular component of the  $\nu_3$  band are attributed to hindered internal rotation exchanging the two equivalent proton-bound structures *via* a planar transition state with  $C_{2v}$  symmetry. The calculated barrier for this internal motion amounts to  $V_b = 202.9 \text{ cm}^{-1}$  and the dimer is closer to the semirigid limit than to free internal rotation. The interpretation of the  $\text{H}_2\text{O}^+$ –He spectrum is supported by the corresponding spectrum of the monodeuterated  $\text{HOD}^+$ –He complex.

## I. Introduction

Intermolecular forces play a key role for important phenomena in chemical physics and biochemistry.<sup>1,2</sup> Ionic complexes isolated in the gas phase are attractive model systems to study ion–ligand interaction potentials both experimentally and theoretically. The fruitful combination of high resolution spectroscopy and quantum-chemical calculations has provided detailed knowledge of the intermolecular potential energy surfaces (PESs) of a variety of small dimers and trimers.<sup>3</sup> The present work reports the infrared (IR) photodissociation spectrum of the ionic  $\text{H}_2\text{O}^+$ –He complex in the vicinity of the symmetric and antisymmetric O–H stretch vibrations of bare  $\text{H}_2\text{O}^+$ ,  $\nu_1$  and  $\nu_3$ . The rotationally resolved spectra provide detailed structural and dynamical information of this open shell dimer in its doublet electronic ground state. The experimental approach is complemented by *ab initio* calculations providing information about regions of the PES which are not accessed by the experiment. So far, only few spectra of ionic He-bearing complexes have been obtained at the level of rotational resolution; these include IR photodissociation spectra of the proton-bound dimers  $\text{OCH}^+$ –He,<sup>4</sup>  $\text{NH}_4^+$ –He,<sup>5</sup>  $\text{N}_2\text{H}^+$ –He,<sup>6</sup>  $\text{OH}^+$ –He,<sup>7</sup>  $\text{NH}_2^+$ –He<sup>8</sup> and the p-bound  $\text{CH}_3^+$ –He complex,<sup>9</sup> a UV photodissociation spectrum of  $\text{N}_2^+$ –He,<sup>10</sup> and a microwave spectrum of  $\text{H}_2^+$ –He.<sup>11</sup>

The  $\text{H}_2\text{O}^+$ –He dimer has been chosen for several reasons. (1) To the best of our knowledge neither experimental nor theoretical studies of  $\text{H}_2\text{O}^+$ –He have been performed prior to the present work. (2) The related  $\text{H}_2\text{O}^+$ –Ar<sup>12,13</sup> and  $\text{H}_2\text{O}^+$ –Ne<sup>14</sup> dimers have previously been investigated using the same experimental and theoretical approaches applied here to  $\text{H}_2\text{O}^+$ –He. The systematic study of  $\text{H}_2\text{O}^+$ –Rg dimers

(Rg = rare gas) provides information about the properties of the intermolecular interaction between  $\text{H}_2\text{O}^+$  and neutral ligands as a function of the interaction strength. Similar to  $\text{H}_2\text{O}^+$ –Ar and  $\text{H}_2\text{O}^+$ –Ne, the  $\text{H}_2\text{O}^+$ –He equilibrium structure is expected to feature a nearly linear proton bond (H-bond). Because induction interactions dominate the attractive part of the PESs of the  $\text{H}_2\text{O}^+$ –Rg dimers,<sup>12</sup> their binding energies are expected to decrease with the polarizability of the Rg atom in the order  $\text{Ar} > \text{Ne} > \text{He}$ . The PES of a  $\text{H}_2\text{O}^+$ –Rg dimer has two equivalent planar H-bond equilibrium structures which are connected *via* hindered internal rotations through potential barriers.<sup>12,14,15</sup> The resulting tunneling splitting depends on the magnitude of the barrier which is expected to decrease with the size of the Rg atom. The absence of tunneling splittings in the spectra of  $\text{H}_2\text{O}^+$ –Ar (at the resolution of  $0.02 \text{ cm}^{-1}$ ) indicates that the internal rotational  $\text{H}_2\text{O}^+$  motions are strongly hindered by large barriers. In contrast, tunneling splittings of the order of  $1 \text{ cm}^{-1}$  have been inferred for  $\text{H}_2\text{O}^+$ –Ne from its IR spectrum.<sup>14</sup> Comparison of  $\text{H}_2\text{O}^+$ –He with other  $\text{AH}_k^+$ –He dimers will reveal the factors influencing the tunneling dynamics in H-bound He complexes featuring multiple equivalent minima. For example, whereas  $\text{NH}_4^+$ –He is close to the free internal rotor limit,<sup>5,16</sup> no signatures of internal rotation have been observed in the IR spectrum of  $\text{HNNH}^+$ –He.<sup>8</sup> (3) Spectroscopic and theoretical studies reveal that the strength of the intermolecular bond in H-bound  $\text{AH}^+$ –Rg dimers is anticorrelated to the difference of the proton affinity (PA) of the two bases A and Rg.<sup>3,13,14,17</sup> Interestingly, the  $\text{HOH}^+$ –Ne and  $\text{HOH}^+$ –Ar complexes have somewhat stronger bonds than would be expected from the published value for  $\text{PA}_{\text{OH}}^+$ .<sup>12–14</sup> This observation has tentatively been attributed to the radical character of the  $\text{H}_2\text{O}^+$  ion

in its doublet electronic ground state and it is anticipated that  $\text{H}_2\text{O}^+-\text{He}$  exhibits the same behaviour. (4) Comparison between the PESs of the  $\text{H}_2\text{O}^+-\text{He}$  cation and the neutral  $\text{H}_2\text{O}-\text{He}$  dimer<sup>18</sup> will reveal the difference in the interaction upon ionization of the molecular subunit. Ionization of  $\text{H}_2\text{O}-\text{He}$  (which is mainly stabilized by dispersion) is expected to have a drastic influence on both the strength and anisotropy of the intermolecular PES owing to the additional induction forces. (5) Finally, the  $\text{H}_2\text{O}^+-\text{He}$  potential is of interest for modeling the chemistry and physics of astrophysical media and terrestrial  $\text{H}_2\text{O}/\text{He}$  plasmas.<sup>19,20</sup>

## II. Experimental

Mid-IR photodissociation spectra of  $\text{H}_2\text{O}^+-\text{He}$  ( $\text{HDO}^+-\text{He}$ ) are recorded in a tandem mass spectrometer described previously.<sup>21,22</sup> The complexes are formed in a cluster ion source combining a pulsed and skimmed supersonic expansion with electron impact ionization. Helium is bubbled at room temperature and 16 bar through a reservoir filled with distilled water and expanded through a pulsed valve into vacuum (a 1 : 1 mixture of  $\text{H}_2\text{O}$  and  $\text{D}_2\text{O}$  is used for the production of  $\text{HDO}^+-\text{He}$ ). The first quadrupole mass spectrometer selects the complexes under study,  $\text{H}_2\text{O}^+-\text{He}$  ( $\text{HDO}^+-\text{He}$ ). Subsequently, the cluster ions are focused into an octopole ion guide where they interact with a counter propagating IR laser pulse. Resonant excitation of intramolecular vibrations of  $\text{H}_2\text{O}^+$  ( $\text{HDO}^+$ ) lying above the dissociation threshold led to dissociation into  $\text{H}_2\text{O}^+$  ( $\text{HDO}^+$ ) and He. No other fragment channels are observed. The produced fragment ions are selected by the second quadrupole mass spectrometer and detected as a function of the laser frequency to obtain the IR action spectra of the dimer ions. Pulsed and tunable IR radiation in the spectral range 2500–6900  $\text{cm}^{-1}$  is generated by an optical parametric oscillator (OPO) laser system. The laser frequency is calibrated by the optoacoustic spectra of ammonia<sup>23</sup> and interpolation between reference lines is facilitated by transmission étalon fringes of the OPO oscillator. The calibrated line positions are corrected for the Doppler shift induced by the kinetic energy of the ions in the octopole ( $E_{\text{kin}} = 6 \pm 1$  eV). Frequent deviation from single mode lasing caused the effective bandwidth of the laser to be about twice the nominal bandwidth of 0.02  $\text{cm}^{-1}$ . Hence, the absolute accuracy of rotational line positions is limited to 0.04  $\text{cm}^{-1}$ . The Doppler width (0.014  $\text{cm}^{-1}$ ) estimated from the uncertainty of the kinetic energy of the ions in the octopole provides only a minor contribution to the observed rotational line width. All spectra are normalized for laser intensity variations measured with an InSb detector.

## III. *Ab initio* calculations

*Ab initio* calculations of  $\text{H}_2\text{O}^+$  and  $\text{H}_2\text{O}^+-\text{He}$  are performed at the unrestricted MP2/aug-cc-pVTZ<sup>#</sup> level of theory.<sup>24</sup> The aug-cc-pVTZ<sup>#</sup> basis set<sup>12</sup> is of similar quality as the aug-cc-pVTZ basis<sup>25</sup> and provides reliable PESs for ionic complexes at the MP2 level.<sup>9,26</sup> The final contraction of the basis is described by (11s7p3d2f)  $\rightarrow$  [7s4p3d2f] for O and (6s3p2d)  $\rightarrow$  [4s3p2d] for H and He. Spin contamination is

negligible in all calculations ( $\langle S^2 \rangle - 0.75 < 0.01$ ). All coordinates are relaxed during the search for stationary points. Interaction energies are first corrected for basis set superposition error (BSSE),<sup>27</sup> and the BSSE corrected energies ( $E_1$ ) are further corrected for the relaxation energy ( $E_2$ ) arising from  $\text{H}_2\text{O}^+$  deformation upon complexation ( $D_e = E_1 - E_2$ ).<sup>28</sup> Harmonic vibrational frequencies are scaled by a factor of 0.942 56 to optimize the agreement between experimental and calculated O–H stretch frequencies of free  $\text{H}_2\text{O}^+$ .<sup>12</sup> The scaled frequencies are used to estimate the zero-point energies and to derive dissociation energies ( $D_0$ ) from the respective well depths ( $D_e$ ). Tables 1–3 and Fig. 1 and 2 summarize the results of the calculations. As the effects of complexation on the monomer normal coordinates are small, the nomenclature of the dimer vibrations refers to the three intramolecular  $\text{H}_2\text{O}^+$  modes ( $\nu_i$ ,  $i = 1-3$ ) and the intermolecular stretching and bending vibrations ( $\nu_s$  and  $\nu_b$ ). The reader is referred to Fig. 3 of ref. 12 for a description of the normal coordinates of the related  $\text{H}_2\text{O}^+-\text{Ar}$  dimer.

The three-dimensional (3-D) intermolecular PES of  $\text{H}_2\text{O}^+-\text{He}$  is studied by keeping the structure of  $\text{H}_2\text{O}^+$  fixed at the optimized monomer geometry and calculating interaction energies for a grid of intermolecular coordinates,  $R$  and  $\gamma_i$  ( $i = 1, 2$ ). Here,  $R$  corresponds to the O–He bond length and  $\gamma_i$  measures the angle between the O–He bond and the  $C_2$  axis of  $\text{H}_2\text{O}^+$  (Fig. 2). Only dimer structures in which the O–He bond lies in one of the two symmetry planes of  $\text{H}_2\text{O}^+$ , corresponding to  $\text{H}_2\text{O}^+$  internal rotation around its  $c$ -axis ( $\gamma_1$ ) or  $a$ -axis ( $\gamma_2$ ), are considered. For each angle  $\gamma_i$  ( $\gamma_i = 0^\circ, 45^\circ, 90^\circ, 135^\circ$  and  $180^\circ$  for  $i = 1, 2$ ), interaction energies are calculated for at least 15 radial points (spaced by 0.1 Å) and least-squares fitted to the 1-D potential  $V(R) = Ae^{-BR} - C(R - D)^{-4}$  ( $A$ ,  $B$ ,  $C$  and  $D$  are fitting parameters). The first term models the exchange repulsion and the second one the induction attraction. The minimum energies,  $D_{\text{min}}$ , and corresponding intermolecular separations,  $R_{\text{min}}$ , of these 1-D radial potential cuts are plotted as functions of  $\gamma_i$  in Fig. 2. Small structural and energetic differences are observed for stationary points calculated by gradient optimization (Tables 1 and 2) and by the rigid monomer approximation (Fig. 2). They arise from the neglect of monomer relaxation in the rigid monomer PES and the fact that the gradient optimization leads to stationary points on the BSSE uncorrected PES, whereas the rigid monomer PES in Fig. 2 is corrected for BSSE.

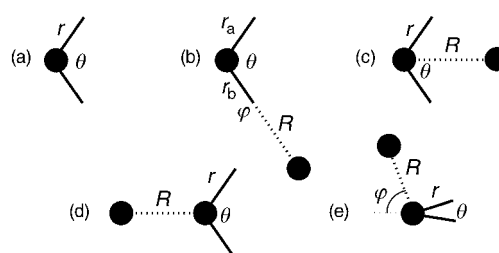


**Fig. 1** Structures of  $\text{H}_2\text{O}^+$  (a,  $C_{2v}$ ) and  $\text{H}_2\text{O}^+-\text{He}$  (b–e) calculated at the UMP2/aug-cc-pVTZ<sup>#</sup> level. The H-bound structure of the dimer (b,  $C_s$ ) is the global minimum, the p-bound structure (c,  $C_s$ ) a local minimum, and the planar bridged (d,  $C_{2v}$ ) and O-bound (e,  $C_{2v}$ ) structures are first and second order saddle points, respectively.

**Table 1** Equilibrium structures (Å, °), rotational constants and energies ( $\text{cm}^{-1}$ ) of  $\text{H}_2\text{O}^+$  and various  $\text{H}_2\text{O}^+-\text{He}$  structures in their electronic ground states calculated at the UMP2/aug-cc-pVTZ<sup>#</sup> level (Fig. 1)

Structure	$r_e$ ( $r_{\text{ao}}/r_{\text{bo}}$ )	$\theta_e/\phi_e$	$R_e$	$A_e$	$B_e$	$C_e$	$E_1$	$E_2$	$D_e/D_0$
$\text{HOH}^+$	0.9980	109.57		28.4378	12.5797	8.7216			
H-bound $\text{H}_2\text{O}^+-\text{He}$	0.9972/1.0009	109.77/173.20	1.6990	21.9308	0.6911	0.6700	426.6	0.7	425.9/158.6
p-bound $\text{H}_2\text{O}^+-\text{He}$	0.9978	109.37/79.78	2.5693	9.1186	0.7732	0.7450	234.5	0.4	234.1/88.0
O-bound $\text{H}_2\text{O}^+-\text{He}$	0.9981	109.51	2.9391	12.5861	0.5594	0.5356	60.6	<0.1	60.6/26.3
bridged $\text{H}_2\text{O}^+-\text{He}$	0.9980	109.11	2.8660	12.6510	0.6411	0.6101	223.9	0.9	223.0/147.4

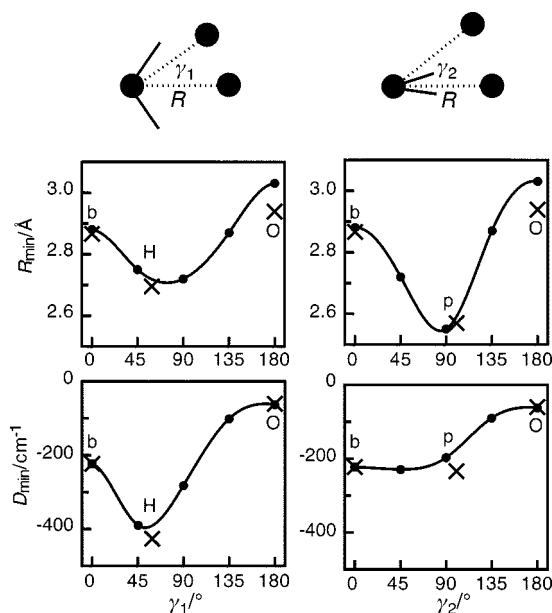


**Fig. 2** Properties of the intermolecular potential energy surface (PES) of  $\text{H}_2\text{O}^+-\text{He}$  calculated at the UMP2/aug-cc-pVTZ<sup>#</sup> level (rigid monomer approximation). The minimal energy separations ( $R_{\min}$ ) are plotted and also the potential energy depths ( $D_{\min}$ ) of 1-D radial cuts through the 3-D PES in (left side) and perpendicular to (right side) the  $\text{H}_2\text{O}^+$  plane as a function of the angles  $\gamma_1$  and  $\gamma_2$ . The calculated data points are interpolated by cubic splines.  $\gamma_1 \sim 59^\circ$  corresponds to the H-bound global minimum (H),  $\gamma_2 \sim 100^\circ$  to the p-bound local minimum (p), and  $\gamma_1 = \gamma_2 = 0^\circ$  and  $\gamma_1 = \gamma_2 = 180^\circ$  to the bridged (b) and O-bound (O) planar transition states. For comparison, the data for stationary points obtained from gradient optimization are included as well (crosses).

The calculated properties of  $\text{H}_2\text{O}^+$  in its  $^2\text{B}_1$  electronic ground state (Fig. 1(a),  $\text{C}_{2v}$ ) are in good agreement with available experimental gas phase and Ne matrix isolation data, as well as previous *ab initio* calculations. The reader is referred to Tables 1 and 2 of ref. 12 for a recent compilation of available experimental and theoretical data for  $\text{H}_2\text{O}^+$  and its deuterated isotopomers.

The global minimum on the  $\text{H}_2\text{O}^+-\text{He}$  PES in Fig. 2 is the planar H-bound  $\text{H}_a-\text{O}-\text{H}_b-\text{He}$  structure (Fig. 1(b),  $\text{C}_s$ ,  $\gamma_1 = 59^\circ$ ). Gradient optimization results in a slightly translinear proton bond with an intermolecular H-He separation of

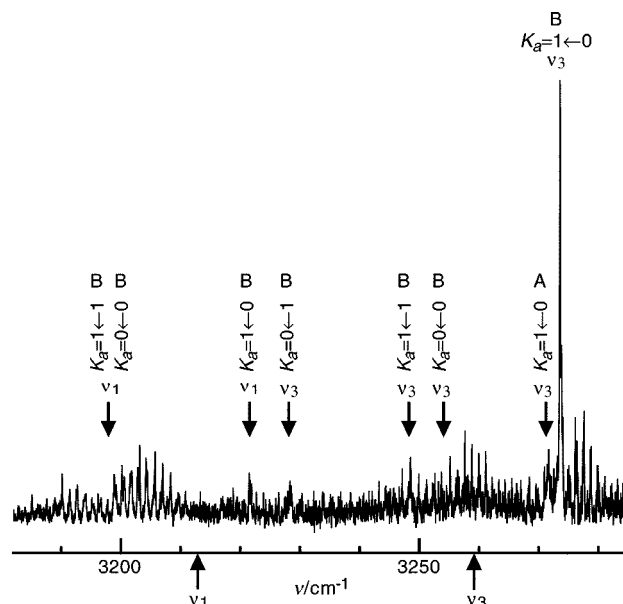


**Fig. 3** Overview of the recorded IR photodissociation spectrum of the  $\nu_1$  and  $\nu_3$  hybrid bands of  $\text{H}_2\text{O}^+-\text{He}$ , along with assignments of the  $\Delta K_a = 0, \pm 1$  subband origins. The arrows below the wavelength scale indicate the frequencies of bare  $\text{H}_2\text{O}^+$ .

$R_e = 1.6990 \text{ \AA}$ , a bond angle of  $\varphi_e = 173.2^\circ$ , and dissociation energies of  $D_e = 425.9$  and  $D_0 = 158.6 \text{ cm}^{-1}$  (Table 1). The effects of complexation on the  $\text{H}_2\text{O}^+$  structure are small (deformation energy  $E_2 = 0.7 \text{ cm}^{-1}$ ) and typical of H-bonding. The bound  $\text{O}-\text{H}_b$  bond elongates ( $\Delta r_{be} = 0.0029 \text{ \AA}$ ), whereas the free  $\text{O}-\text{H}_a$  bond contracts slightly ( $\Delta r_{ae} = -0.0008 \text{ \AA}$ ). The HOH bond angle is nearly unaffected ( $\Delta\theta_e = 0.2^\circ$ ). The complexation-induced frequency shifts of the intramolecular  $\text{H}_2\text{O}^+$  modes are consistent with these structural changes. In bare  $\text{H}_2\text{O}^+$  both O-H local oscillators are equivalent and the resonant interaction between them gives rise to the symmetric and antisymmetric O-H stretch normal modes,  $\nu_1$  and  $\nu_3$ . H-bonding to He weakens the  $\text{O}-\text{H}_b$  and strengthens the  $\text{O}-\text{H}_a$  bond. Thus, the degeneracy of the two O-H local oscillators is removed upon complexation and the coupling between the two local modes is reduced. As a consequence, the  $\nu_1$  and  $\nu_3$  modes of the complex are better described as bound and free O-H stretch modes, although the

**Table 2** Scaled harmonic vibrational frequencies ( $\text{cm}^{-1}$ ) of  $\text{H}_2\text{O}^+$  and various  $\text{H}_2\text{O}^+-\text{He}$  structures in their electronic ground states calculated at the UMP2/aug-cc-pVTZ<sup>#</sup> level (Fig. 1)<sup>a</sup>

Structure	Nature <sup>b</sup>	$\nu_1$	$\nu_2$	$\nu_3$	$\nu_s$	$\nu_b$	$\nu_b$
$\text{HOH}^+ (^2\text{B}_1/\text{C}_{2v})$	GM	3206.7 (a <sub>1</sub> /124)	1384.0 (a <sub>1</sub> /172)	3265.1 (b <sub>2</sub> /491)			
H-bound $\text{H}_2\text{O}^+-\text{He} (^2\text{A}''/\text{C}_s)$	GM	3172.3 (a'/320)	1388.3 (a'/157)	3253.5 (a'/461)	186.2 (a'/67)	166.1 (a'/76)	224.0 (a''/163)
p-bound $\text{H}_2\text{O}^+-\text{He} (^2\text{A}''/\text{C}_s)$	LM	3209.6 (a'/120)	1387.4 (a'/167)	3267.1 (a''/479)	93.4 (a'/76)	156.8 (a'/341)	33.7 (a''/18)
O-bound $\text{H}_2\text{O}^+-\text{He} (^2\text{B}_1/\text{C}_{2v})$	SP2	3205.3 (a <sub>1</sub> /126)	1385.3 (a <sub>1</sub> /172)	3263.5 (b <sub>2</sub> /488)	70.3 (a <sub>1</sub> /11)	55.3i (b <sub>1</sub> /370)	63.6i (b <sub>2</sub> /97)
bridged $\text{H}_2\text{O}^+-\text{He} (^2\text{B}_1/\text{C}_{2v})$	SP1	3209.1 (a <sub>1</sub> /128)	1384.6 (a <sub>1</sub> /190)	3263.6 (b <sub>2</sub> /470)	112.3 (a <sub>1</sub> /13)	37.5 (b <sub>1</sub> /400)	112.1i (b <sub>2</sub> /136)

<sup>a</sup> Vibrational symmetries and IR intensities ( $\text{km mol}^{-1}$ ) are listed in parentheses. <sup>b</sup> GM = global minimum; LM = local minimum; SPn = stationary point with n imaginary frequencies.

**Table 3** Scaled harmonic vibrational frequencies and dissociation energies ( $\text{cm}^{-1}$ ) of H-bound  $\text{H}_2\text{O}^+-\text{He} (^2\text{A}''/\text{C}_s)$  and its deuterated isotopomers calculated at the UMP2/aug-cc-pVTZ<sup>#</sup> level (Fig. 1)<sup>a</sup>

Structure	$\nu_1$ (a')	$\nu_2$ (a')	$\nu_3$ (a')	$\nu_s$ (a')	$\nu_b$ (a')	$\nu_b$ (a'')	$D_0$
$\text{HOH}^+-\text{He}$	3172.3 (320)	1388.3 (157)	3253.5 (461)	186.2 (67)	166.1 (76)	224.0 (163)	158.6
$\text{DOH}^+-\text{He}$	3181.4 (495)	1224.7 (119)	2359.2 (129)	182.8 (23)	142.2 (70)	223.6 (179)	170.2
$\text{HOD}^+-\text{He}$	2312.6 (213)	1211.2 (121)	3245.8 (322)	183.4 (31)	139.7 (64)	162.9 (62)	199.4
$\text{DOD}^+-\text{He}$	2289.4 (112)	1016.7 (61)	2383.8 (263)	182.0 (20)	124.2 (48)	162.4 (76)	206.8

<sup>a</sup> Vibrational symmetries and IR intensities ( $\text{km mol}^{-1}$ ) are listed in parentheses.



decoupling is less pronounced than in  $\text{H}_2\text{O}^+-\text{Ne}$  and  $\text{H}_2\text{O}^+-\text{Ar}$ . The net effect of strengthening/weakening of the  $\text{O}-\text{H}_{\text{a/b}}$  bonds and reducing the coupling leads to the frequency shifts,  $\Delta\nu_1 = -34.4 \text{ cm}^{-1}$  and  $\Delta\nu_3 = -11.6 \text{ cm}^{-1}$ . The significant enhancement of the  $\nu_1$  intensity upon H-bonding (factor 2.5) causes both O–H stretch modes of  $\text{H}_2\text{O}^+-\text{He}$  to have comparable IR oscillator strengths. Approximating  $\text{H}_2\text{O}^+-\text{He}$  by a diatomic, the scaled intermolecular stretching frequency ( $\nu_s = 186.2 \text{ cm}^{-1}$ ) corresponds to a harmonic force constant of  $k_s = 6.7 \text{ N m}^{-1}$ . The two intermolecular bending frequencies are calculated as  $\nu_b(\text{a}') = 166.1 \text{ cm}^{-1}$  and  $\nu_b(\text{a}'') = 224.0 \text{ cm}^{-1}$ . All vibrational frequencies of the H-bound structure are positive and real, confirming that this geometry is a minimum on the PES (Table 2). Table 3 lists the frequencies and binding energies of H-bound  $\text{HOH}^+-\text{He}$  and its deuterated isotopomers. The effects of sequential deuteration are similar to those observed for  $\text{HOH}^+-\text{Ar}$  and  $\text{HOH}^+-\text{Ne}$  and have been discussed in detail in ref. 12. Two monodeuterated isomers exist, H-bound  $\text{DOH}^+-\text{He}$  and D-bound  $\text{HOD}^+-\text{He}$ , and they can readily be distinguished by their characteristic O–H/D stretching frequencies. In general, deuteration tends to reduce the frequencies and IR intensities of the modes sensitive to deuteration, whereas the dissociation energies increase slightly (Table 3).

The planar bridged  $\text{H}_2\text{O}^+-\text{He}$  structure (Fig. 1(c),  $C_{2v}$ ,  $\gamma_1 = \gamma_2 = 0^\circ$ ) is a transition state for interconversion of the two equivalent H-bound global minima *via* hindered internal rotation of  $\text{H}_2\text{O}^+$  around its *c*-axis (Fig. 2). The barrier for this hindered motion is calculated as  $V_b = 202.9 \text{ cm}^{-1}$ . The frequency of the in-plane bending mode,  $\nu_b(\text{b}_2)$ , is large and imaginary, confirming that the bridged structure is a first order transition state. The planar O-bound structure (Fig. 1(d),  $C_{2v}$ ,  $\gamma_1 = \gamma_2 = 180^\circ$ ) is also a transition state for hindered internal rotation of  $\text{H}_2\text{O}^+$  around its *c*-axis, however the barrier is considerably higher,  $V_b = 365.3 \text{ cm}^{-1}$ . Moreover, both the in-plane and out-of-plane bending frequencies are imaginary, indicating that the interaction increases when the He atom is moving toward the H-bound or the bridged structure (Fig. 2). Fig. 2 suggests a shallow p-bound local minimum near  $\gamma_2 = 90^\circ$  in which the He atom is attached to the singly occupied  $2p_y$  orbital of oxygen. Indeed, searches using gradient optimization located such a minimum (Fig. 1(e),  $C_s$ ,  $\gamma_2 = 100.2^\circ$ ,  $\phi_e = 79.8^\circ$ ). Similar to  $\text{H}_2\text{O}^+-\text{Ne}$ ,<sup>14</sup> the PES is very flat along the  $\gamma_2$  coordinate in this region. This is in contrast to  $\text{H}_2\text{O}^+-\text{Ar}$ , where the p-bound structure is a pronounced local minimum with significant stabilization arising from partial charge transfer from Ar to the  $2p_y$  orbital of oxygen (the  $^2\text{B}_1$  electronic state of  $\text{H}_2\text{O}^+$  has an unpaired electron in the  $\text{b}_1$  molecular orbital, which closely corresponds to the  $2p_y$  out-of-plane atomic orbital of O).<sup>12</sup> Apparently, this charge transfer is largely suppressed in the case of He and Ne, probably because of their much higher ionization potentials.<sup>29</sup> The calculated binding energy of the p-bound local minimum,  $D_e = 234.1 \text{ cm}^{-1}$ , provides an estimate for  $\text{H}_2\text{O}^+$  internal rotation around its *b*-axis,  $V_b = 191.8 \text{ cm}^{-1}$ . The structural, energetic and vibrational properties of the bridged, O-bound, and p-bound structures are summarized in Tables 1 and 2. As the intermolecular interaction in all three structures is weaker than for the global H-bound minimum, the perturbation of the  $\text{H}_2\text{O}^+$  monomer upon complexation is correspondingly smaller. In particular, the frequency shifts of  $\nu_1$  and  $\nu_3$  (which for symmetry reasons remain symmetric and antisymmetric O–H stretch modes) are less pronounced ( $|\Delta\nu_{1,3}| < 3 \text{ cm}^{-1}$ ).

The charge distributions of the stationary points are analyzed using the atoms-in-molecules (AIM) approach to investigate the nature of the  $\text{H}_2\text{O}^+-\text{He}$  intermolecular interaction as a function of the orientation.<sup>24</sup> Similar to  $\text{H}_2\text{O}^+-\text{Ne}$ ,<sup>14</sup> the attraction in  $\text{H}_2\text{O}^+-\text{He}$  is dominated for all

orientations by induction forces between the charge distribution of  $\text{H}_2\text{O}^+$  and the polarizability of the Rg atom. The charge transfer mechanism, which provides additional stabilization of the p-bound  $\text{H}_2\text{O}^+-\text{Ar}$  structure ( $q_{\text{Ar}} = 0.11 e$ ),<sup>12</sup> is not operative in  $\text{H}_2\text{O}^+-\text{He}$  and  $\text{H}_2\text{O}^+-\text{Ne}$ . The AIM charges and induced dipole moments of the H-bound  $\text{H}_2\text{O}^+-\text{He}$  equilibrium structure are  $q_{\text{Ha}} = 0.762 e$ ,  $q_{\text{Hb}} = 0.767 e$ ,  $q_{\text{O}} = -0.535 e$ ,  $q_{\text{He}} = 0.007 e$  and  $\mu_{\text{He}} = 0.065 \text{ D}$ . The transferred charge and induced dipole are smaller for the p-bound local minimum ( $q_{\text{He}} = 0.002 e$ ,  $\mu_{\text{He}} = 0.045 \text{ D}$ ) leading to the weaker interaction.

## IV. Results and discussion

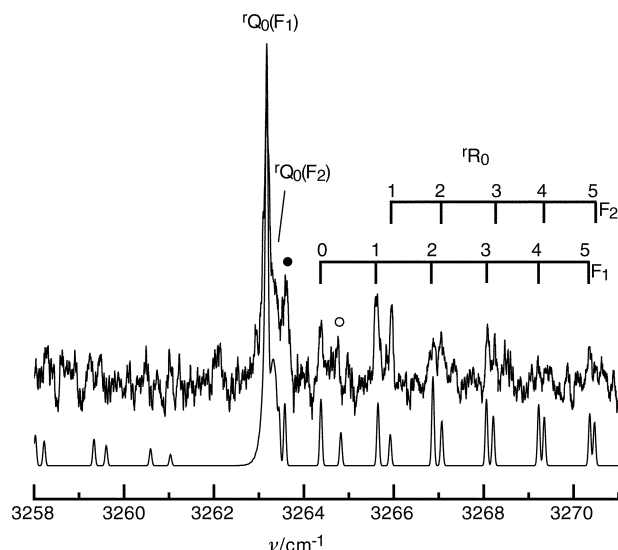
### 1. Vibrational analysis

Fig. 3 shows the photodissociation spectrum of  $\text{H}_2\text{O}^+-\text{He}$  recorded in the range of the O–H stretch fundamentals of free  $\text{H}_2\text{O}^+$  ( $\nu_1 = 3212.86 \text{ cm}^{-1}$ ,  $\nu_3 = 3259.04 \text{ cm}^{-1}$ ).<sup>30</sup> Within the scanned range ( $3175\text{--}3330 \text{ cm}^{-1}$ ) two strong hybrid bands centered at  $\sim 3198$  and  $\sim 3254 \text{ cm}^{-1}$  with rotational structures appropriate for a nearly symmetric prolate top are observed. Based upon the comparison with the *ab initio* calculations, they are assigned to the  $\nu_1$  and  $\nu_3$  fundamentals of a H-bound  $\text{H}_2\text{O}^+-\text{He}$  dimer. As outlined in Section III, the  $\nu_1$  mode has more bound O–H<sub>b</sub> stretch character than  $\nu_3$  and features thus a significant red shift,  $\Delta\nu_1 = -15 \text{ cm}^{-1}$ . In contrast,  $\nu_3$  has more free O–H<sub>a</sub> stretch character and the red shift is correspondingly smaller,  $\Delta\nu_3 = -5 \text{ cm}^{-1}$ . In general, the observed shifts are in qualitative agreement with the *ab initio* calculations ( $\Delta\nu_1 = -34.4 \text{ cm}^{-1}$ ,  $\Delta\nu_3 = -11.6 \text{ cm}^{-1}$ ). In accord with the analysis of the normal coordinates of H-bound  $\text{H}_2\text{O}^+-\text{He}$ , the parallel component of  $\nu_1$  ( $\Delta K_a = 0$ ) is much more intense than the perpendicular component ( $\Delta K_a = \pm 1$ ), whereas both components of  $\nu_3$  have comparable intensities. In the spectra of  $\text{H}_2\text{O}^+-\text{Ne}$  and  $\text{H}_2\text{O}^+-\text{Ar}$ , the  $\Delta K_a = \pm 1$  subbands of  $\nu_1$  are not observed,<sup>13,14</sup> as in these dimers this mode is nearly a pure bound O–H stretch vibration with the transition dipole lying almost parallel to the *a*-axis.<sup>12</sup>

IR spectra of  $\text{HDO}^+-\text{Rg}$  with  $\text{Rg} = \text{Ar}^{13}$  and  $\text{Ne}^{14}$  show absorptions of both possible isomers of the monodeuterated dimer in the range of the O–H stretch fundamentals: the free O–H stretch of D-bound  $\text{HOD}^+-\text{Rg}$  ( $\nu_3$ ) and the bound O–H stretch of H-bound  $\text{DOH}^+-\text{Rg}$  ( $\nu_1$ ). Both isotopomers of the corresponding complex with He have comparable binding energies (Table 3) and are thus expected to be produced in similar abundance in the present ion source. However, low signal-to-noise ratios allow only the observation of the prominent  $K_a = 1 \leftarrow 0$  subband of the  $\nu_3$  fundamental of  $\text{HOD}^+-\text{He}$  (Q branch at  $3263.3 \text{ cm}^{-1}$ , Fig. 4). The deuteration-induced red shift of  $\sim -10 \text{ cm}^{-1}$  from the corresponding Q branch of  $\text{H}_2\text{O}^+-\text{He}$  is consistent with calculated shift of the  $\nu_3$  fundamental for this isotopomer of  $-7.7 \text{ cm}^{-1}$ .

### 2. Hindered internal rotation

The tunneling motion between the two equivalent H-bound minima on the  $\text{H}_2\text{O}^+-\text{Rg}$  dimer PES splits each rotational level with  $A'$  ( $A''$ ) symmetry in the molecular symmetry group  $C_s$  (rigid structure) into two levels with  $A_1 + B_2$  ( $A_2 + B_1$ ) symmetry in the molecular symmetry group  $G_4$  (isomorphic to  $C_{2v}$ , nonrigid structure). The magnitude of the splitting depends sensitively on the details of the tunneling pathway (*e.g.*, path length and barrier height). It may also depend significantly on the degree of rovibrational excitation. Owing to the  $^2A''$  ( $^2B_1$ ) symmetry of the electronic ground state of  $\text{H}_2\text{O}^+-\text{Rg}$ , the lowest rovibrational level splits into a lower lying  $B_1$  and a higher lying  $A_2$  component which are symmetric and antisymmetric in the tunneling coordinate. The



**Fig. 4** Expanded view of the  $K_a = 1 \leftarrow 0$  subband of the  $v_3$  fundamental of the D-bound  $\text{HOD}^+\text{-He}$  dimer with assignments and a simulation using the constants in Table 4, a temperature of 30 K, and a convolution width of  $0.06 \text{ cm}^{-1}$ . The full and open circles indicate the  $Q(1) F_2$  and the forbidden  $R(0) F_2 \leftarrow F_1$  transitions.

selection rules for IR allowed transitions are  $A_1 \leftrightarrow A_2$  and  $B_1 \leftrightarrow B_2$  and the nuclear spin statistical weights are 1 and 3 for levels with A and B symmetry, respectively.<sup>31</sup> The  $v_1$  and  $v_3$  vibrations have  $a_1$  and  $b_2$  symmetry, giving rise to the following splittings in their IR spectra (Fig. 5): the difference (sum) of the tunneling splittings in the ground and excited vibrational states is observed for the parallel (perpendicular) subbands of  $v_1$  and the perpendicular (parallel) subbands of  $v_3$ . In contrast to  $\text{H}_2\text{O}^+\text{-Rg}$ , no tunneling splitting occurs for the monodeuterated dimers, due to the lack of two equivalent equilibrium configurations on the PES.

To estimate the order of magnitude of the tunneling splitting in the ground vibrational state of  $\text{H}_2\text{O}^+\text{-He}$ , two tunneling paths are considered: hindered rotation of  $\text{H}_2\text{O}^+$  around its  $c$ -axis (in-plane) and its  $b$ -axis (out-of-plane). In both cases, the 1-D Schrödinger equation is solved<sup>32</sup> using a potential derived by fitting the *ab initio* PES (Fig. 2) along the minimum energy path to the following expansion:

$$V(\phi) = \sum_n \frac{V_n}{2} (1 - \cos(n\phi)) \quad (1)$$

The effective internal rotor constants are approximated by the  $\text{H}_2\text{O}^+$  rotational constants ( $B_0 = 12.42 \text{ cm}^{-1}$ ,  $C_0 = 8.47$

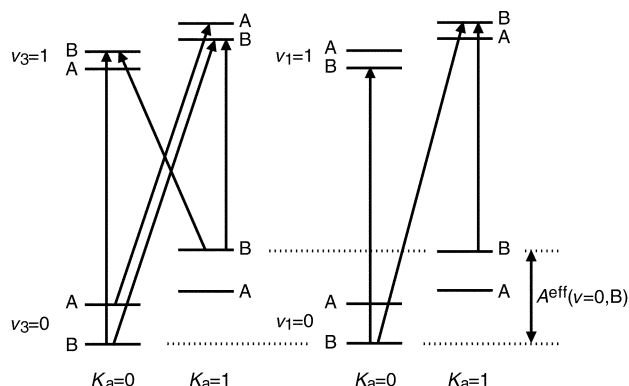


**Fig. 5** Qualitative energy level diagram for the A and B tunneling components of the  $K_a = 0$  and 1 levels of the ground,  $v_1$ , and  $v_3$  vibrational states of  $\text{H}_2\text{O}^+\text{-He}$ . The arrows indicate subband transitions observed in Fig. 3.

$\text{cm}^{-1}$ ).<sup>33</sup> The potential for the in-plane rotation is characterized by  $V_1 = -284.35$ ,  $V_2 = -139.17$ ,  $V_3 = 123.86$  and  $V_4 = -32.98 \text{ cm}^{-1}$  and the corresponding ground state tunneling splitting amounts to  $\Delta_0 = 0.64 \text{ cm}^{-1}$ . The potential for the out-of-plane rotation has a twofold barrier,  $V_2 = 200 \text{ cm}^{-1}$ , giving rise to  $\Delta_0 = 0.26 \text{ cm}^{-1}$ . Thus, according to the simple 1-D model the in-plane path produces the larger splitting. As the model is based upon several approximations, it provides only qualitative values for the splittings. 3-D calculations are likely to yield larger splittings, as the additional zero-point energy contributions reduce the “effective” barrier.

Analysis of the  $v_1$  and  $v_3$  spectra reveals mainly the observation of the more intense B tunneling components of the  $\Delta K_a = 0$  and  $\Delta K_a = \pm 1$  subbands (Fig. 3 and 5). These include  $K_a = 0 \leftarrow 0$  ( $3253.9 \text{ cm}^{-1}$ ),  $1 \leftarrow 1$  ( $3248.5 \text{ cm}^{-1}$ ),  $0 \leftarrow 1$  ( $3228.1 \text{ cm}^{-1}$ ), and  $1 \leftarrow 0$  ( $3274.4 \text{ cm}^{-1}$ ) of  $v_3$ , and  $1 \leftarrow 1$  ( $3196.3 \text{ cm}^{-1}$ ),  $0 \leftarrow 0$  ( $3198.0 \text{ cm}^{-1}$ ) and  $1 \leftarrow 0$  ( $3222.3 \text{ cm}^{-1}$ ) of  $v_1$  (given are the positions of subband origins). These assignments are confirmed by three independent determinations of the energy difference between the  $K_a = 0$  and  $K_a = 1$  levels (B components) of the ground vibrational state, yielding all the same value  $A^{\text{eff}}(v=0, B) = 25.86 \pm 0.15 \text{ cm}^{-1}$  (Fig. 5). This value corresponds to the structural  $A_0$  molecular constant modified by the effect of the tunneling splittings in the  $K_a = 0$  and  $K_a = 1$  states,  $A^{\text{eff}}(v=0, B) = A_0 + (\Delta_0^{K_a=0} + \Delta_0^{K_a=1})/2$ . Inspection of the  $v_3$   $K_a = 1 \leftarrow 0$  subband of  $\text{H}_2\text{O}^+\text{-He}$  (Fig. 3 and 6) reveals a weak feature at  $3271.7 \text{ cm}^{-1}$  which is attributed to the Q branch of the less intense A tunneling component. The observed intensity ratio of the two Q branches with A and B symmetry ( $\sim 1 : 6$ ) deviates somewhat from the value expected from the nuclear spin statistical weights ( $1 : 3$ ). The splitting between the two Q branches of  $1.9 \text{ cm}^{-1}$  corresponds to the decrease of the tunneling splitting upon  $v_3$   $K_a = 1 \leftarrow 0$  excitation. Thus, the ground state splitting,  $\Delta_0^{K_a=0}$ , has to be larger than  $1.9 \text{ cm}^{-1}$ . Assuming that the splitting is independent of  $K_a$  ( $\Delta_0^{K_a=0} = \Delta_0^{K_a=1}$ ) and estimating  $A_0$  from the calculated  $A_e$  constant of the H-bound equilibrium structure ( $A_e = 21.9 \text{ cm}^{-1}$ ,  $A_0 \sim 22.5$ ),<sup>12,13</sup> the ground state splitting is estimated as  $\Delta_0 \sim 3.4 \text{ cm}^{-1}$ . As expected, this value is somewhat larger than the calculated splittings using the 1-D model,  $\Delta_0 = 0.64 \text{ cm}^{-1}$ . It also implies that the tunneling splitting in the  $v_3$  state is largely reduced ( $\Delta_3 \sim 1.5 \text{ cm}^{-1}$ ). Moreover,  $A^{\text{eff}}(v_3 = 1, B) = 20.5 \text{ cm}^{-1}$  and  $\Delta_3 \sim 1.5 \text{ cm}^{-1}$  yield the structural  $A$  molecular constant in the  $v_3$  state,  $A_3 \sim 22.0 \text{ cm}^{-1}$ , which is smaller than  $A_0 = 22.5 \text{ cm}^{-1}$ , because  $v_3$  excitation involves an effective lengthening of the free O–H<sub>a</sub> bond.<sup>13</sup> Assuming that  $A_1 \sim A_0$ , the value of  $A^{\text{eff}}(v_1 = 1, B) = 24.3 \text{ cm}^{-1}$  corresponds to a splitting in the  $v_1$  state,  $\Delta_1 = 1.7 \text{ cm}^{-1}$ , that is similar to  $\Delta_3$ . Thus, excitation of both  $v_1$  and  $v_3$  reduces the tunneling probability. This scenario is similar to  $\text{H}_2\text{O}^+\text{-Ne}$ , where the ground state splitting ( $\Delta_0^{K_a=0} > 0.43 \text{ cm}^{-1}$ ) is also significantly reduced upon  $v_3$  excitation:  $\Delta_0 = 1.0 \text{ cm}^{-1}$  and  $\Delta_3 = 0.6 \text{ cm}^{-1}$  are obtained under the same assumptions. A strong intramolecular mode dependence of the tunneling dynamics in dimers is often observed (e.g., HF–HF).<sup>34</sup> In addition, the  $\text{H}_2\text{O}^+\text{-Ne}$   $v_3$  spectrum indicates that the splitting depends not only on vibrational excitation, but also on  $K_a$ .<sup>14</sup> Unfortunately, selection rules prevented the separation of both effects using the available data set for  $\text{H}_2\text{O}^+\text{-He}$  and  $\text{H}_2\text{O}^+\text{-Ne}$ ,<sup>14</sup> as well as for the related  $\text{H}_2\text{O}\text{-CO}$  dimer.<sup>35–38</sup>

### 3. Rotational analysis

Both the  $v_1$  and  $v_3$  bands of  $\text{H}_2\text{O}^+\text{-He}$  display rotational structure in their P and R branches. For the rovibrational analysis a standard semirigid Hamiltonian appropriate for a prolate symmetric top ( $\kappa_c = -0.9980$  for H-bound  $\text{H}_2\text{O}^+\text{-He}$ ) in a doublet electronic state is employed, including terms for vibration, rotation and centrifugal distortion, and spin–

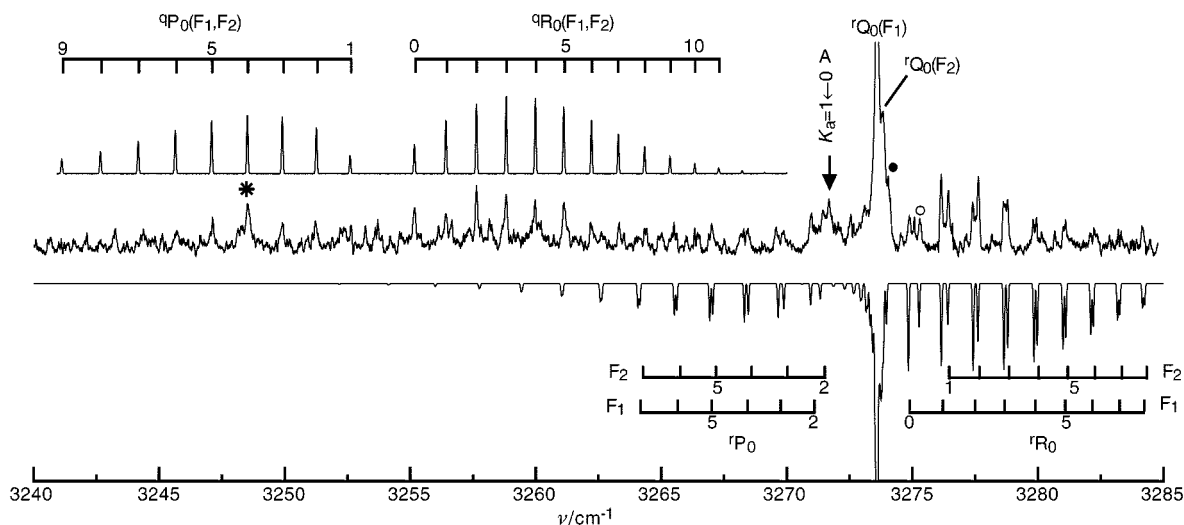


**Fig. 6** Expanded view of the  $\nu_3$  band of  $\text{H}_2\text{O}^+-\text{He}$  with assignments and separate simulations of the  $K_a = 0 \leftarrow 0$  and  $K_a = 1 \leftarrow 0$  subbands (B components) using the constants in Table 4, a temperature of 30 K, and a convolution width of  $0.06 \text{ cm}^{-1}$ . The full and open circles indicate the  $Q(1) F_2$  and the forbidden  $R(0) F_2 \leftarrow F_1$  transitions, and the asterisk the Q branch of the  $K_a = 1 \leftarrow 1$  subband (B component).

rotation interaction:<sup>13,39,40</sup>

$$\begin{aligned} \hat{H} = & \nu_0 + \bar{B}\hat{N}^2 + (A - \bar{B})\hat{N}_z^2 \pm \frac{1}{4}(B - C)\hat{N}^2\delta_{K_a1} \\ & - D_N\hat{N}^4 - D_{NK}\hat{N}^2\hat{N}_z^2 - D_K\hat{N}_z^4 \\ & + a_0(\hat{N}_x\hat{S}_x + \hat{N}_y\hat{S}_y + \hat{N}_z\hat{S}_z) \\ & + a(2\hat{N}_z\hat{S}_z - \hat{N}_x\hat{S}_x - \hat{N}_y\hat{S}_y). \end{aligned} \quad (2)$$

The term  $\pm \frac{1}{4}(B - C)\hat{N}^2\delta_{K_a1}$  accounts for the asymmetry splitting in the  $K_a = 1$  states (into  $c$  and  $d$  parity doublets),  $\bar{B} = (B + C)/2$ , and  $a_0$  and  $a$  describe the spin-rotation interaction in the  $^2A''$  electronic ground state of  $\text{H}_2\text{O}^+-\text{He}$ . The spin-rotation parameters  $a$  and  $a_0$  ( $b = 0$  for a symmetric top) can be transformed to the equivalent set of  $\varepsilon_{ii}$  parameters ( $i = a, b, c$ ), which may be more convenient for comparison with the respective  $\text{H}_2\text{O}^+$  parameters ( $\varepsilon_{aa} = -a_0 - 2a$ ,  $\varepsilon_{bb} = \varepsilon_{cc} = -a_0 + a$ ).<sup>40</sup> According to Hund's case (b), the rotational angular momentum  $\hat{N}$  couples with the electron spin  $\hat{S}$  to form the total angular momentum  $\hat{N}$ . For  $S = 1/2$  each  $N \neq 0$  level is split into two components with  $J = N + 1/2$  ( $F_1$ ) and  $J = N - 1/2$  ( $F_2$ ). The selection rules for allowed transitions are  $F_i \leftrightarrow F_i$  ( $i = 1, 2$ ),  $\Delta J = 0, \pm 1$  and  $\Delta J = \Delta N$ . Furthermore, the selection rules for an  $a$ -type parallel transition are  $\Delta K_a = 0, ++ \leftrightarrow ++$  and  $+- \leftrightarrow +-$ , whereas for a  $b$ -type perpendicular transition  $\Delta K_a = \pm 1, ++ \leftrightarrow --$  and  $+- \leftrightarrow +-$ .

Effects arising from tunneling necessitate separate least-squares fits for each tunneling component of the  $\nu_1$  and  $\nu_3$   $\Delta K_a = 0, \pm 1$  subbands of  $\text{H}_2\text{O}^+-\text{He}$  to Hamiltonian (2). Consequently, the molecular constants  $A$ ,  $D_{NK}$  and  $D_K$  cannot be determined and are set to zero in the respective fits. The molecular constants for the  $K_a = 0 \leftarrow 0$  and  $K_a = 1 \leftarrow 0$  subbands of  $\nu_3$  (B components) listed in Table 4 are obtained from the following 68 rotational transitions:  $^{\Delta K_a}\Delta N_{K_a}(N) = {}^1P_0(2-8)$ ,  ${}^1R_0(0-8)$ ,  ${}^1P_0(0-10)$ ,  ${}^1R_0(0-10)$ , the  $F_2$  component of  ${}^1Q_0(1)$  and the forbidden ( $\Delta J \neq \Delta N$ ) transition  ${}^1R_0(0) F_2 \leftarrow F_1$ . A list of all peak positions is available upon request. As Q branch and P/R branch transitions connect different levels of the asymmetry doublets, the asymmetry term ( $B - C$ ) is required to reproduce the experimental Q branch position of the  $K_a = 1 \leftarrow 0$  subband at  $3273.6 \text{ cm}^{-1}$  (fwhm =  $0.5 \text{ cm}^{-1}$ ). The assignments in the  $K_a = 0 \leftarrow 0$  subband are determined by comparing combination differences for  $K_a = 0$  with those of the  $K_a = 1 \leftarrow 0$  subband. The fits for  $K_a = 1 \leftarrow 0$  and  $K_a = 0 \leftarrow 0$  have standard deviations of  $\sigma = 0.025$  and  $0.028 \text{ cm}^{-1}$ , compatible with the spectral resolution ( $0.03 \text{ cm}^{-1}$ ). The molecular constants listed in Table 4 reproduce all experimental line positions to within  $0.07 \text{ cm}^{-1}$ . Fig. 6 compares the

experimental  $\nu_3$  spectrum of  $\text{H}_2\text{O}^+-\text{He}$  to a simulation of the B components using the constants in Table 4, a temperature of  $T = 30 \text{ K}$  and a convolution width of  $0.06 \text{ cm}^{-1}$ . The Q branches of the B components of the  $K_a = 1 \leftarrow 1$  and  $K_a = 0 \leftarrow 1$  subbands are centered at  $3248.5$  and  $3228.4 \text{ cm}^{-1}$ , and the Q branch of the A component of the  $K_a = 1 \leftarrow 0$  subband occurs at  $3271.7 \text{ cm}^{-1}$ . Although P and R branch lines of these subbands are present in the experimental spectrum (Fig. 6), low signal-to-noise ratios and/or spectral congestion prevent unambiguous assignments and a detailed rotational analysis.

Eleven rotational lines of the  $K_a = 1 \leftarrow 0$  subband of the  $\nu_3$  fundamental of  $\text{HOD}^+-\text{He}$  (Fig. 4) are used to determine the molecular constants listed in Table 4:  $^{\Delta K_a}\Delta N_{K_a}(N) = {}^1R_0(0-5) F_1$ ,  ${}^1R_0(1-3) F_2$ , the  $F_2$  component of  ${}^1Q_0(1)$  and the forbidden ( $\Delta J \neq \Delta N$ ) transition  ${}^1R_0(0) F_2 \leftarrow F_1$ . Again, the asymmetry parameter  $B - C$  is necessary to reproduce the position of the unresolved Q branch at  $3263.3 \text{ cm}^{-1}$  (fwhm  $0.5 \text{ cm}^{-1}$ ). Fig. 4 compares the experimental spectrum to a simulation using the constants in Table 4, a temperature of  $T = 30 \text{ K}$  and a convolution width of  $0.06 \text{ cm}^{-1}$ . Assuming an  $A$  rotational constant of  $A' = 21.0 \pm 0.5 \text{ cm}^{-1}$ , the band origin is estimated as  $3243.6 \pm 0.5 \text{ cm}^{-1}$ .

The parallel component of  $\nu_1$  of  $\text{H}_2\text{O}^+-\text{He}$  consists of overlapping  $\Delta K_a = 0$  subbands of the A and B tunneling components (Fig. 7). An unambiguous assignment of the observed

**Table 4** Molecular constants of the  $K_a = 1 \leftarrow 0$  and  $K_a = 0 \leftarrow 0$  subbands of the  $\nu_3$  vibration of  $\text{H}_2\text{O}^+-\text{He}$  (B tunneling component) and  $\text{HOD}^+-\text{He}$  derived from fitting rovibrational line positions to Hamiltonian (2). Standard deviations are given in parentheses

Constant/ $\text{cm}^{-1}$	HOH $^+-\text{He}$		HOD $^+-\text{He}$
	$K_a = 0 \leftarrow 0$	$K_a = 1 \leftarrow 0$	$K_a = 1 \leftarrow 0$
$\bar{B}''$	0.6535 <sup>a</sup>	0.6535(14)	0.632(14)
$\bar{B}'$	0.638 84(14)	0.6473(14)	0.625(13)
$B'-C' (\times 10^2)$		1.60(31)	1.7(10)
$D_N'' (\times 10^5)$	0.0 <sup>a</sup>	2.3(16)	0.0 <sup>a</sup>
$D_N' (\times 10^5)$	0.0 <sup>a</sup>	5.9(12)	0.0 <sup>a</sup>
$e_{aa}''$		−0.523(34)	−0.562(46)
$e_{bb}'' + e_{cc}'' (\times 10^2)$	−3.0(19)	−3.2(21)	0.0 <sup>a</sup>
$e_{bb}' + e_{cc}' (\times 10^2)$	−2.8(19)	−3.2(21)	0.0 <sup>a</sup>
$\nu_0^b$	3253.9086(74)	3274.361(12)	3263.926(25)
Lines used	38	30	11
$\sigma (\times 10^2)$	2.8	2.5	3.0

<sup>a</sup> Fixed in the fit. <sup>b</sup> Absolute accuracy of calibration is  $0.04 \text{ cm}^{-1}$ .



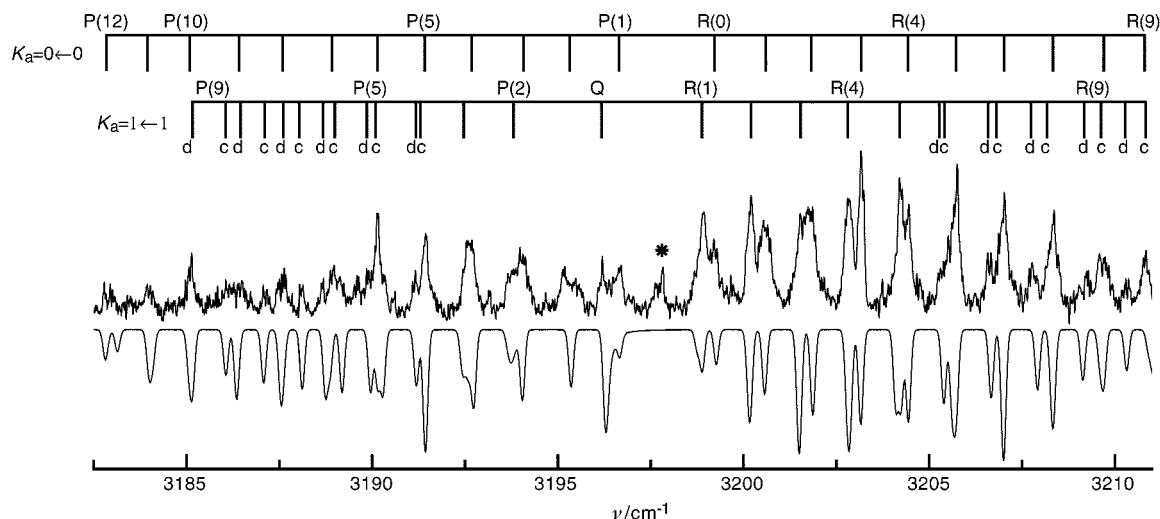


**Fig. 7** Expanded view of the  $\nu_1$  band of  $\text{H}_2\text{O}^+-\text{He}$  including the suggested assignments and separate simulations of the  $K_a = 0 \leftarrow 0$  and  $K_a = 1 \leftarrow 1$  subbands (B components) using the constants in Table 6, a temperature of 30 and 60 K for  $K_a = 0$  and 1, and a convolution width of  $0.15 \text{ cm}^{-1}$ . The peak indicated by the asterisk is tentatively attributed to the  $K_a = 1 \leftarrow 1$  Q branch with A symmetry.

rotational transitions (Table 5) to the individual subbands is not possible at the present stage. Nevertheless, the origin of the B tunneling component of the  $K_a = 1 \leftarrow 1$  subband can be estimated as  $3196.4 \pm 0.3 \text{ cm}^{-1}$  from the difference of the  $K_a = 1 \leftarrow 0$  subband origin and  $A^{\text{eff}}(v = 0, \text{B})$  determined from the  $\nu_3$  transition (Fig. 5). Moreover, assuming that  $\nu_1$  excitation reduces the tunneling splitting (similar to  $\nu_3$ ), the origin of the  $\nu_1$   $K_a = 0 \leftarrow 0$  subband (B component) is expected to occur at higher frequency than the  $K_a = 1 \leftarrow 1$  subband (Fig. 5). The tentative assignments of the B tunneling components of these two subbands ( $K_a = 0 \leftarrow 0$  and  $K_a = 1 \leftarrow 1$ ) in Fig. 7 and Table 5 are consistent with these considerations. Separate fits of the two subbands resulted in the molecular constants listed in Table 6. As the spin-rotation splitting is not resolved, the corresponding parameters in Hamiltonian (2) are set to zero. The band origins are  $3197.97(3) \text{ cm}^{-1}$  and  $3196.28(3) \text{ cm}^{-1}$  for  $K_a = 0 \leftarrow 0$  and  $K_a = 1 \leftarrow 1$ , the latter being in good agreement with the estimated value of  $3196.4 \pm 0.3 \text{ cm}^{-1}$ . Fig. 7 compares the experimental  $\nu_1$  spectrum of  $\text{H}_2\text{O}^+-\text{He}$  with separate simulations of the  $K_a = 0 \leftarrow 0$  and  $K_a = 1 \leftarrow 1$  sub-

bands (B component) using the molecular constants in Table 6, temperatures of  $T = 30 \text{ K}$  ( $K_a = 0$ ) and  $T = 60 \text{ K}$  ( $K_a = 1$ ) and a convolution width of  $0.15 \text{ cm}^{-1}$ . There remain unassigned peaks which probably arise from the weaker A tunneling components of both  $\Delta K_a = 0$  subbands: for example, the peak at  $3197.8 \text{ cm}^{-1}$  (indicated in Fig. 7 by an asterisk) may be attributed to the Q branch of the  $K_a = 1 \leftarrow 1$  subband.

The width of individual rotational lines in single scans of the  $\nu_3$  bands of  $\text{H}_2\text{O}^+-\text{He}$  and  $\text{HOD}^+-\text{He}$  are limited by the effective bandwidth of the IR laser ( $\sim 0.03 \text{ cm}^{-1}$ ), providing a lower limit for the lifetime of the  $\nu_3$  vibrational state,  $\tau_3 > 170 \text{ ps}$ . The widths of the lines in the  $\nu_1$  spectrum are typically  $> 0.1 \text{ cm}^{-1}$  and significantly broader than the laser bandwidth. This is mainly attributed to spectral congestion arising from unresolved spin-rotation interaction and asymmetry doublets as well as overlapping  $\Delta K_a = 0$  subbands (A and B tunneling components). It can, however, not be excluded that part of the broadening arises from fast energy redistribution and/or dissociation. Hence, only a lower limit for the  $\nu_1$  lifetime can be estimated as  $\tau_1 > 50 \text{ ps}$ .

**Table 5** Rotational line positions ( $\text{cm}^{-1}$ ) of the parallel component of the  $\nu_1$  band with the suggested assignments<sup>a</sup>

	$K_a = 0 \leftarrow 0$	$K_a = 1 \leftarrow 1$		$K_a = 0 \leftarrow 0$	$K_a = 1 \leftarrow 1$
P(1)	3196.67		Q		3196.20
P(2)	3195.48	3193.80	R(0)	3199.20	
P(3)	3194.06	3192.54	R(1)	3200.58	3198.92
P(4)	3192.69	3191.44(c)	R(2)	3201.81	3200.20
		3191.16(d)			
P(5)	3191.44	3190.14(c)	R(3)	3203.16	3201.52
		3189.90(d)			
P(6)	3190.14	3189.13(c) <sup>b</sup>	R(4)	3204.45	3202.80
		3188.67(d) <sup>b</sup>			
P(7)	3188.97	3188.10(c)	R(5)	3205.70	3204.12(d)
		3187.56(d)			3204.23(c)
P(8)	3187.56	3187.12(c)	R(6)	3206.97	3205.38(d)
		3186.46(d) <sup>b</sup>			3205.70(c)
P(9)	3186.46 <sup>b</sup>	3186.10(c) <sup>b</sup>	R(7)	3208.36	3206.61(d)
		3185.15(d)			3206.97(c)
P(10)	3185.15	3185.15(c)	R(8)	3209.68	3207.78(d)
		3184.03(d)			3208.36(c)
P(11)	3184.03	3184.03(c)	R(9)	3210.80	3209.24(d)
					3209.68(c)
P(12)	3182.95				

<sup>a</sup> Positions are accurate to  $\pm 0.05 \text{ cm}^{-1}$ . The splittings arising from asymmetry doubling ((c) and (d)) are resolved for some transitions.

<sup>b</sup> Not included in the fit.

#### 4. Structure and dissociation energy

The rovibrational analysis of the IR spectrum of  $\text{H}_2\text{O}^+-\text{He}$  (e.g., vibrational frequency shifts and IR intensities, rotational constants, tunneling splittings, nuclear spin statistical weights, deuteration shifts) is only consistent with a nearly linear H-bound equilibrium structure, in agreement with the *ab initio* PES. It is not compatible with other possible geometries,

**Table 6** Molecular constants of the  $K_a = 0 \leftarrow 0$  and  $K_a = 1 \leftarrow 1$  subbands of the  $\nu_1$  vibration of  $\text{H}_2\text{O}^+-\text{He}$  (B tunneling component) derived from fitting rovibrational line positions in Table 5 to Hamiltonian (2). Standard deviations are given in parentheses

Constant/ $\text{cm}^{-1}$	$K_a = 0 \leftarrow 0$	$K_a = 1 \leftarrow 1$
$\bar{B}''$	0.6535 <sup>a</sup>	0.6272(11)
$\bar{B}'$	0.6516(12)	0.6370(18)
$B''-C'' (\times 10^2)$		3.52(43)
$B'-C' (\times 10^2)$		1.82(42)
$D_N'' (\times 10^5)$	6.36(62)	2.3 <sup>a</sup>
$D_N' (\times 10^5)$	3.8(14)	5.0(14)
$\nu_0^b$	3197.969(26)	3196.279(28)
Lines used	21	34
$\sigma (\times 10^2)$	5.7	7.2

<sup>a</sup> Fixed in the fit. <sup>b</sup> Absolute accuracy of calibration is  $0.04 \text{ cm}^{-1}$ .

such as the p-bound, bridged or O-bound structures. For example, the  $A$  rotational constant extracted from the separation of the  $\Delta K_a = 0$  and  $\Delta K_a = \pm 1$  subbands of  $v_1$  and  $v_3$  is of the order of  $\sim 22 \text{ cm}^{-1}$ , indicating that one proton is close to the line connecting the two heavy atoms. As is evident from Fig. 5, the  $A$  rotational constant is influenced to some extent by the tunneling splitting and can not be employed to derive quantitative structural parameters. In contrast, the  $B$  and  $C$  rotational constants may be used to roughly estimate the geometry of the intermolecular bond assuming a rigid dimer structure. For this purpose, the  $\text{H}_2\text{O}^+$  geometry in  $\text{H}_2\text{O}^+-\text{He}$  is assumed to adopt the experimental  $\text{H}_2\text{O}^+$  structure ( $r_0 = 0.999 \text{ \AA}$ ,  $\theta = 110.5^\circ$ ),<sup>30</sup> modified by the calculated structural changes upon He complexation, yielding  $r_a = 0.9982 \text{ \AA}$ ,  $r_b = 1.0019 \text{ \AA}$  and  $\theta = 110.7^\circ$ . Under these assumptions,  $\bar{B} = 0.6535(14) \text{ cm}^{-1}$  results in an intermolecular separation in the ground vibrational state (B component) of  $R_0 = 1.756(4) \text{ \AA}$  and a bond angle  $\varphi_0 = 176(9)^\circ$ . Assuming further an  $A_0$  constant of  $22(1) \text{ cm}^{-1}$  ( $A_e = 21.9 \text{ cm}^{-1}$ , Table 1), the derived intermolecular bond parameters are  $R_0 = 1.756(4) \text{ \AA}$  and  $\varphi_0 = 175(5)^\circ$ . The obtained bond angle is in agreement with the calculated value,  $\varphi_e = 173.2^\circ$ . As expected, the experimental  $R_0$  value is somewhat larger than the calculated  $R_e$  value ( $R_e = 1.699 \text{ \AA}$ ), mainly due to the zero-point motion of the intermolecular stretching mode. In addition, the tunneling dynamics may also contribute to the  $R_0 - R_e$  difference, because the  $R_e$  value calculated for the bridged structure ( $R_{\text{O-He}} = 2.8660 \text{ \AA}$ ,  $\bar{B} = 0.6256 \text{ cm}^{-1}$ ) is larger than for the H-bound structure ( $R_{\text{O-He}} = 2.6955 \text{ \AA}$ ,  $\bar{B} = 0.6806 \text{ cm}^{-1}$ ). Moreover, the calculated asymmetry of the H-bound structure,  $B_e - C_e = 0.0211 \text{ cm}^{-1}$ , is in fair agreement with the experimental value,  $B_0 - C_0 = 0.0160(31) \text{ cm}^{-1}$ . The rotational constants of  $\text{HOD}^+-\text{He}$  are not influenced by the tunneling motion and correspond to intermolecular parameters,  $R_0 = 1.794(35) \text{ \AA}$  and  $\varphi_0 = 174(5)^\circ$ , that are very similar to those derived for  $\text{H}_2\text{O}^+-\text{He}$ .

The calculations predict ground state dissociation energies of  $D_e = 425.9 \text{ cm}^{-1}$  and  $D_0 = 158.6 \text{ cm}^{-1}$ , i.e. the zero-point energy amounts to 63% of the well depth using the rather crude harmonic approximation. The calculated harmonic force constant of the intermolecular bond is  $k_s = 6.7 \text{ N m}^{-1}$ . The complexation induced frequency red shifts,  $\Delta v_1 = -15$  and  $\Delta v_3 = -5.1 \text{ cm}^{-1}$ , correspond to the increase in the intermolecular interaction upon vibrational excitation of 9 and 3%, respectively. The increase is larger for  $v_1$ , because it contains more bound O–H stretch character than  $v_3$ . In general, excitation of the proton donor stretch modes in H-bound dimers leads to a significant stabilization of the intermolecular bond (Section V.2).<sup>3</sup>

## V. Comparison of related complexes

### 1. Comparison of $\text{H}_2\text{O}^+-\text{Rg}$

The  $\text{H}_2\text{O}^+-\text{Rg}$  dimers with  $\text{Rg} = \text{He}$ ,  $\text{Ne}^{14}$  and  $\text{Ar}^{12,13}$  have been studied systematically with the same experimental and theoretical techniques and thus allow a detailed comparison of the interaction parameters as a function of the bond strength. Table 7 summarizes several calculated and experimental properties of the three considered  $\text{H}_2\text{O}^+-\text{Rg}$  dimers. The PESs of all three dimers feature a slightly translinear, planar H-bound equilibrium structure. The strength ( $D_e$ ,  $D_0$ ,  $k_s$ ) and length ( $R_e$ ,  $R_0$ ) of the intermolecular bond increases in the order  $\text{He} < \text{Ne} < \text{Ar}$ , whereas the deviation from linearity ( $180^\circ - \varphi_e$ ) decreases. The attractive part of the intermolecular potential near the H-bound equilibrium is dominated by the induction interaction between the positive charge distribution of  $\text{H}_2\text{O}^+$  and the polarizability of the Rg atom,  $\alpha_{\text{Rg}}$ , which induces a dipole moment,  $\mu_{\text{Rg}}$ .<sup>12</sup> Approximating  $\text{H}_2\text{O}^+$  by a point charge,  $q$ , the charge-induced dipole interaction is

**Table 7** Comparison of several structural, vibrational and energetic properties of H-bound  $\text{H}_2\text{O}^+-\text{Rg}$  complexes derived from *ab initio* calculations (c) and IR spectra (e)

	$\text{H}_2\text{O}^+-\text{He}$	$\text{H}_2\text{O}^+-\text{Ne}^a$	$\text{H}_2\text{O}^+-\text{Ar}^b$
$\Delta r_a/\text{\AA}$ (c)	−0.0008	−0.0020	−0.0041
$\Delta r_{bc}/\text{\AA}$ (c)	0.0029	0.0058	0.0289
$\Delta \theta_e/^\circ$ (c)	0.20	0.28	0.43
$R_e/\text{\AA}$ (c)	1.6990	1.7745	1.9154
$R_0/\text{\AA}$ (e)	1.756(4)	1.815(5)	1.929(15)
$\varphi_e/^\circ$ (c)	173.20	174.16	176.08
$\varphi_0/^\circ$ (e)	175(5)	174(4)	175(4)
$D_e/\text{cm}^{-1}$ (c)	425.9	756.0	2484.3
$D_0/\text{cm}^{-1}$ (c)	158.6	476.4	2194.6
$E_2/\text{cm}^{-1}$ (c)	0.7	4.7	121.5
$q_{\text{Rg}}/e$ (c)	0.007	0.013	0.059
$\mu_{\text{Rg}}/D$ (c)	0.065	0.118	0.366
$V_b/\text{cm}^{-1}$ (c)	202.9	340.5	1110.4
$v_s/\text{cm}^{-1}$ (c)	186.2	144.5	207.4
$k_s/\text{N m}^{-1}$ (c)	6.7	11.7	31.5
$\Delta v_1/\text{cm}^{-1}$ (c)	−34	−87	−477
$\Delta v_1/\text{cm}^{-1}$ (e)	−15	−69	−541
$\Delta v_3/\text{cm}^{-1}$ (c)	−12	−3	17
$\Delta v_3/\text{cm}^{-1}$ (e)	−5	−6	25
$\Delta v_1^c/\text{cm}^{-1}$ (e) <sup>c</sup>	−38	−92	−564
$\Delta v_3^c/\text{cm}^{-1}$ (e) <sup>c</sup>	18	17	48
$\tau_1/\text{ps}$ (e)	> 50	> 250	$10 \pm 5$
$\tau_3/\text{ps}$ (e)	> 170	> 250	> 250

<sup>a</sup> Ref. 14. <sup>b</sup> Ref. 12 and 13. <sup>c</sup> Frequency shifts with respect to the center frequency,  $\nu_c = 3235.95 \text{ cm}^{-1}$ .

given by  $V_{\text{CID}} = -\alpha_{\text{Rg}} q^2 R^{-4}$ . The AIM population analysis reveals only small changes of the  $\text{H}_2\text{O}^+$  charge distribution upon Rg complexation. For example only a small charge transfer from the Rg atom to  $\text{H}_2\text{O}^+$  is predicted (0.007, 0.013, 0.059  $e$  for He, Ne, Ar). Hence, assuming that the total interaction,  $D_e$ , is proportional to the attraction,  $V_{\text{CID}}$ , the product of  $D_e R_e^4$  is anticipated to be proportional to  $\alpha_{\text{Rg}}$ . This expectation is confirmed by the data:  $D_e R_e^4$  varies as 1.0 : 2.1 : 9.4 for He : Ne : Ar and  $\alpha_{\text{Rg}}$  as 1.0 : 2.0 : 8.1 ( $\alpha_{\text{Rg}} = 0.2, 0.39$  and  $1.63 (4\pi\epsilon_0) \text{ \AA}^3$  for He, Ne and Ar).<sup>41</sup> Within this simple induction model, the product  $\mu_{\text{Rg}} R_e^2$ , is also proportional to  $\alpha_{\text{Rg}}$  and this trend is indeed observed:  $\mu_{\text{Rg}} R_e^2$  varies as 1.0 : 2.0 : 7.2 for He : Ne : Ar. In addition to the radial bond strength, the anisotropy of the  $\text{H}_2\text{O}^+-\text{Rg}$  PES increases with the size of the Rg atom. The calculated barriers for internal rotation *via* the planar bridged transition state,  $V_b = 202.9, 340.5$  and  $1110.4 \text{ cm}^{-1}$  for Rg = He, Ne and Ar, are in all three cases approximately  $\sim 45\text{--}48\%$  of the respective  $D_e$  values. Consequently, the topology of the PESs near the H-bound geometries is very similar, with the interaction strength scaling with  $\alpha_{\text{Rg}}$ . As the effective hindered rotation constants are similar in all three  $\text{H}_2\text{O}^+-\text{Rg}$  dimers, the calculated tunneling splittings drastically increase with smaller Rg size ( $\Delta_0 = 0.64, 0.34$  and  $0.002 \text{ cm}^{-1}$  for He, Ne and Ar).

The relaxation energy  $E_2$  is a measure of the complexation-induced changes of the  $\text{H}_2\text{O}^+$  geometry and increases with the interaction strength of H-bound  $\text{H}_2\text{O}^+-\text{Rg}$ . The structural changes include the significant lengthening of the bound O–H<sub>b</sub> bond ( $\Delta r_{bc}$ ), the much smaller contraction of the free O–H<sub>a</sub> bond ( $\Delta r_{ae}$ ) and the slight increase of the HOH bond angle ( $\Delta \theta_e$ ). These effects are also monitored in the frequency shifts,  $\Delta v_1$  and  $\Delta v_3$ . The experimental  $v_1$  and  $v_3$  frequencies of  $\text{H}_2\text{O}^+-\text{Rg}$  are plotted in Fig. 8 as a function of  $\alpha_{\text{Rg}}$ . In the following discussion, a simple two-state model is employed to rationalize the magnitude and direction of the frequency shifts listed in Table 7. In free  $\text{H}_2\text{O}^+$ , the resonant interaction between the two degenerate local O–H stretch oscillators leads to the formation of symmetric and antisymmetric O–H stretch normal modes. Both modes are split by  $46.2 \text{ cm}^{-1}$  around the center frequency ( $\nu_c = 3236.0 \text{ cm}^{-1}$ ). The latter fre-



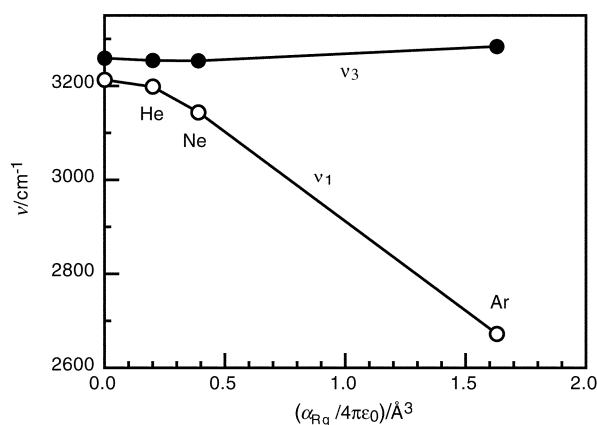


**Fig. 8** Plot of the experimental  $\nu_1$  and  $\nu_3$  frequencies of  $\text{H}_2\text{O}^+-\text{Rg}$  as a function of  $\alpha_{\text{Rg}}$  ( $\alpha_{\text{Rg}}/4\pi\epsilon_0 = 0.2, 0.39$  and  $1.63 \text{ \AA}^3$  for He, Ne and Ar).<sup>41</sup>

quency is characteristic for the O–H bond strength in free  $\text{H}_2\text{O}^+$  and the splitting corresponds to twice the off-diagonal coupling matrix element ( $V = 23.1 \text{ cm}^{-1}$ ). Complexation with a Rg atom significantly reduces the strength of the bound O–H<sub>b</sub> bond, whereas the free O–H<sub>a</sub> bond becomes slightly stronger, thereby lifting the degeneracy of the two local modes. The normal modes in the dimer can now be described as bound and free O–H stretch local modes with  $\nu_b \ll \nu_c$  and  $\nu_f > \nu_c$ . As a result, the coupling  $V$  is reduced upon complexation. Thus, there are two effects determining  $\Delta\nu_1$  and  $\Delta\nu_3$ . (I) Strengthening (weakening) of the O–H<sub>a</sub> (O–H<sub>b</sub>) bonds tends to increase (decrease)  $\nu_3$  ( $\nu_1$ ), whereas (II) the smaller coupling tends to decrease (increase)  $\nu_3$  ( $\nu_1$ ). The dominating effect depends on the interaction strength. For the limit of strong intermolecular binding (*e.g.*, Rg = Ar), the decoupling of the two modes is almost complete and effect (I) leads to a large negative  $\Delta\nu_1$  and a small positive  $\Delta\nu_3$ . In the limit of weak bonding (Rg = He), the coupling is still substantial, leading to small negative (and more similar) values for both  $\Delta\nu_1$  and  $\Delta\nu_3$ . From Table 7 it is evident that both the experimental and theoretical frequency shifts reproduce the trends derived from this simple two-state model. The calculations significantly overestimate the frequency shifts for Rg = He (but slightly underestimate them for Rg = Ar). In the former complex, the tunneling dynamics cause the ground state wave function to sample regions of the PES (*e.g.*, the bridged transition state) with smaller calculated shifts, which may account for this apparent difference.

The shifts,  $\Delta\nu_1$  and  $\Delta\nu_3$ , reflect directly the changes in the  $\text{H}_2\text{O}^+-\text{Rg}$  binding energy ( $D_0$ ) upon  $\nu_1$  and  $\nu_3$  excitation. Excitation of  $\nu_1$  causes a significant increase of the interaction and a contraction of the intermolecular bond:  $\Delta\nu_1/D_e$  amounts of  $-3.5$ ,  $-9.1$  and  $-21.8\%$  for Rg = He, Ne and Ar;  $\Delta R_0 \sim -0.015$  and  $-0.05 \text{ \AA}$  for Ne and Ar. In contrast, excitation of  $\nu_3$  has almost no effect on the interaction strength:  $\Delta\nu_3/D_e = -1.2$ ,  $-0.8$  and  $+1.0\%$  for Rg = He, Ne and Ar. The difference in the magnitude of  $\Delta\nu_1$  and  $\Delta\nu_3$  is large for Rg = Ne and Ar, implying that the two O–H stretch modes are nearly decoupled leading to almost pure bound and free O–H stretch normal modes in the dimers. In contrast, the coupling remains significant in  $\text{H}_2\text{O}^+-\text{He}$ . Mono-deuteration leads in all cases to nearly complete decoupling into O–H and O–D stretch modes (Table 8). The free O–H stretch modes of D-bound  $\text{HOD}^+-\text{Rg}$  display blue shifts of 7.6, 14 and  $50.5 \text{ cm}^{-1}$  from  $\nu_c = 3236 \text{ cm}^{-1}$  for complexation with Rg = He, Ne and Ar, which reflect the contraction of the free O–H<sub>a</sub> bond. These blue shifts correspond to 1.8, 1.9 and 2.0% of the  $\text{HOD}^+-\text{Rg}$  binding energies ( $D_e$ ), *i.e.* they are roughly proportional to the intermolecular bond strength. The bound O–H stretch of H-bound  $\text{DOH}^+-\text{Rg}$  has only

**Table 8** Experimental frequencies of O–H stretch fundamentals of  $\text{HOD}^+-\text{Rg}$  and  $\text{DOH}^+-\text{Rg}$ <sup>a</sup>

	$\nu_1/\text{cm}^{-1}$	$\nu_3/\text{cm}^{-1}$
$\text{HOD}^+-\text{He}$		3243.6 (7.6, $-10$ )
$\text{HOD}^+-\text{Ne}^b$		$3250 \pm 2$ (14, $-3$ )
$\text{DOH}^+-\text{Ne}^b$	$3144 \pm 2$ ( $-92$ , $\sim 0$ )	
$\text{HOD}^+-\text{Ar}^c$		3286.5 (50.5, 2.6)
$\text{DOH}^+-\text{Ar}^c$	$2688.5 \pm 1$ ( $-547.5$ , 16)	

<sup>a</sup> Frequency shifts with respect to the center frequency,  $\nu_c = 3235.95 \text{ cm}^{-1}$ , and the  $\nu_{1,3}$  fundamentals of  $\text{H}_2\text{O}^+$  are given in parentheses.

<sup>b</sup> Ref. 14. <sup>c</sup> Ref. 13.

been observed for Rg = Ne and Ar and the red shifts of  $-92$  and  $-547.5 \text{ cm}^{-1}$  from  $\nu_c$  amount to 12.2 and 22.0% of the binding energy. The shift of the free O–H stretch frequency upon deuteration of the bound proton is much larger for Rg = He ( $-10 \text{ cm}^{-1}$ ) than for Ne and Ar ( $-3$  and  $3 \text{ cm}^{-1}$ ), confirming that for  $\text{H}_2\text{O}^+-\text{He}$  only deuteration leads to a nearly complete decoupling of the O–H/D stretch modes, whereas in  $\text{H}_2\text{O}^+-\text{Ne}$  and  $\text{H}_2\text{O}^+-\text{Ar}$  already complexation reduces the coupling to a large extent.

The lifetimes of the  $\nu_1$  and  $\nu_3$  vibrational states in  $\text{H}_2\text{O}^+-\text{Rg}$  dimers,  $\tau_1$  and  $\tau_3$ , provide information about the coupling strengths between the O–H stretch modes and the intermolecular degrees of freedom.<sup>3,42–44</sup> In general, the larger this coupling, the larger the frequency shift, and the shorter the lifetime with respect to dissociation. Thus,  $\tau_1$  is anticipated to be shorter than  $\tau_3$ , as the bound O–H stretch couples more efficiently to the dissociation continuum than the free O–H stretch. Moreover,  $\tau_1$  is expected the decrease in the order He > Ne > Ar, as the bond strength and  $\Delta\nu_1$  increases in the same order. The experimental lifetimes listed in Table 7 are consistent with such a view.

## 2. Comparison with $\text{H}_2\text{O}-\text{Rg}$ and $\text{AH}^+-\text{He}$

*Ab initio* calculations and spectroscopic data for neutral  $\text{H}_2\text{O}-\text{Rg}$  dimers (Rg = He,<sup>18</sup> Ne,<sup>45</sup> Ar,<sup>46</sup> Kr<sup>47</sup>) reveal that these systems are mainly stabilized by dispersion forces (in contrast to the cation dimers in which the attraction is based upon induction). The  $\text{H}_2\text{O}-\text{Rg}$  binding energies are 32, 45, and  $143 \text{ cm}^{-1}$  for Rg = He, Ne and Ar. The weak bonding in  $\text{H}_2\text{O}-\text{Rg}$  leads to barriers to internal rotation that are comparable to the  $\text{H}_2\text{O}$  rotational constants. Thus, the bonding in the neutral dimers is much weaker and less directional than in the corresponding cation dimers. Whereas the neutral  $\text{H}_2\text{O}-\text{Rg}$  complexes are close to the free internal rotor limit,  $\text{H}_2\text{O}^+-\text{Rg}$  dimers are better described as substantially hindered internal rotors. Comparison of  $\text{H}_2\text{O}^+-\text{He}$  and  $\text{H}_2\text{O}-\text{He}$  reveals directly the changes in the PES upon ionization. The PES of  $\text{H}_2\text{O}-\text{He}$  calculated at the MP4 level has a planar, non H-bonded global minimum ( $R = 3.15 \text{ \AA}$ ,  $\gamma_1 = 105^\circ$ ,  $D_e = 31.8 \text{ cm}^{-1}$ ) with barriers of  $10\text{--}20 \text{ cm}^{-1}$  for in-plane and out-of-plane internal rotation. Apparently, the interaction in the neutral system is not only weaker and more isotropic than in the cation dimer, but the topology of the PES is also drastically different.

Table 9 summarizes selected properties of H-bound  $\text{AH}^+-\text{He}$  complexes investigated with the same experimental and theoretical tools. The intermolecular interaction strength in these dimers depends upon the difference of the proton affinity (PA) of the two bases A and He.<sup>3,13,14,17</sup> Table 9 compares the binding energies calculated at the MP2/aug-cc-pVTZ<sup>#</sup> level ( $D_e$ ) as well as the experimental values for the intermolecular H–He separation ( $R_0$ ) and the relative red shift of the A–H stretch frequency ( $|\Delta\nu_1/\nu_1|$ ) as a function of  $\text{PA}_A$ .<sup>19,48</sup> In general, the larger  $\text{PA}_A$ , the weaker and longer

**Table 9** Selected properties of H-bound  $\text{AH}^+ - \text{He}$  dimers

$\text{AH}^+$	$\text{SiOH}^{+a}$	$\text{OCH}^{+b}$	$\text{HOH}^+$	$\text{HNH}^{+c}$	$\text{OCOH}^{+d}$	$\text{N}_2\text{H}^{+e}$	$\text{OH}^{+f}$	$\text{O}_2\text{H}^{+g}$	$\text{NH}_4^{+h}$
$\text{PA}_k/\text{kJ mol}^{-1}$	779	594	593	590	541	494	485	421	854
$D_e/\text{cm}^{-1}$	190	242	426	273	396	483	618		148
$ \Delta v_1/v_1 (\%)$	0.2	0.4	1.2 (0.5) <sup>i</sup>		1.4	2.3	2.2	$3.8 \pm 1.3$	
$R_0/\text{\AA}$		2.00	1.76	1.90		1.72	1.62		

<sup>a</sup> Ref. 17. <sup>b</sup> Ref. 4 and 17. <sup>c</sup> Ref. 8. <sup>d</sup> Ref. 49. <sup>e</sup> Ref. 6 and 17. <sup>f</sup> Ref. 7 and 17. <sup>g</sup> Ref. 50. <sup>h</sup> Ref. 16. <sup>i</sup> 1.2 and 0.5% are the relative red shifts from  $v_e$  and  $v_1$ , respectively.

the intermolecular bond and the smaller the monomer perturbation and  $|\Delta v_1/v_1|$ . However, similar to  $\text{H}_2\text{O}^+ - \text{Ne}$  and  $\text{H}_2\text{O}^+ - \text{Ar}$ ,<sup>13,14</sup> the  $\text{H}_2\text{O}^+ - \text{He}$  interaction is somewhat stronger than expected from  $\text{PA}_{\text{OH}}$ . This effect has tentatively been attributed to the radical character of  $\text{H}_2\text{O}^+$  in the doublet electronic ground state (all other considered  $\text{AH}^+$  ions have either singlet or triplet ground states).<sup>12</sup> Alternatively, the experimental value for  $\text{PA}_{\text{OH}}$  may be in error.<sup>19</sup>

Finally, the tunneling dynamics in H-bound  $\text{AH}_k^+ - \text{He}$  dimers is considered ( $\text{AH}_k^+ = \text{NH}_4^+, \text{NH}_2^+$  and  $\text{H}_2\text{O}^+$ ). The tunneling probability for  $\text{AH}_k^+ - \text{He}$  ( $k > 1$ ) depends on the barrier height ( $V_b$ ), the angle separating equivalent minima on the PES ( $\rho_b$ ), and the effective internal rotor constant ( $b$ ). The larger  $b$  and the smaller  $V_b$  and  $\rho_b$ , the larger the calculated tunneling splitting in the ground vibrational state ( $\Delta_0$ ). The large PA of  $\text{NH}_3$  causes the  $\text{NH}_4^+ - \text{He}$  bond to be relatively weak ( $D_e = 148 \text{ cm}^{-1}$ ).<sup>16</sup> The resulting small internal rotation barrier ( $V_b \sim 20 \text{ cm}^{-1}$ ), together with the short tunneling pathway ( $\rho_b = 109^\circ$ ) explains why  $\text{NH}_4^+ - \text{He}$  ( $b = 5.93 \text{ cm}^{-1}$ ) displays almost free internal rotation ( $\Delta_0 = 12.4 \text{ cm}^{-1}$ ).<sup>5,16</sup> In contrast, the quasilinear  $\text{HNH}^+ - \text{He}$  is close to the semirigid bender limit, because the barrier, the internal rotor constant, and the path length are larger ( $D_e = 273 \text{ cm}^{-1}$ ,  $V_b = 156 \text{ cm}^{-1}$ ,  $b = 7.96 \text{ cm}^{-1}$ ,  $\rho_b = 180^\circ$ ,  $\Delta_0 \sim 0.1 \text{ cm}^{-1}$ ).<sup>8</sup> The  $\text{H}_2\text{O}^+ - \text{He}$  dimer constitutes an intermediate case, with  $D_e = 426 \text{ cm}^{-1}$ ,  $V_b = 203 \text{ cm}^{-1}$ ,  $b = 8.47 \text{ cm}^{-1}$ ,  $\rho_b = 118^\circ$ ,  $\Delta_0 = 0.64 \text{ cm}^{-1}$ .

## VI. Concluding remarks

The present work reports the first spectroscopic and quantum chemical characterization of the  $\text{H}_2\text{O}^+ - \text{He}$  dimer. Rotationally resolved IR spectra of the O–H stretch fundamentals provide central information about the structural and dynamical parameters of the intermolecular interaction. As expected, the attraction is based upon induction forces and the complex is less strongly bound and more flexible than the previously characterized  $\text{H}_2\text{O}^+ - \text{Ne}$  and  $\text{H}_2\text{O}^+ - \text{Ar}$  dimers. The experimental intermolecular bond parameters in the ground vibrational state of  $\text{H}_2\text{O}^+ - \text{He}$ ,  $R_0 = 1.756(4) \text{ \AA}$  and  $\varphi_0 = 175(5)^\circ$ , are in good agreement with the calculated values. The observed tunneling splittings arising from hindered internal  $\text{H}_2\text{O}^+$  rotation ( $\sim 3\text{--}4 \text{ cm}^{-1}$ ) are significantly larger than estimated values from 1-D model calculations employing the *ab initio* PES ( $< 1 \text{ cm}^{-1}$ ). Clearly, a better quality *ab initio* PES and/or multidimensional rovibrational calculations are required for a better quantitative agreement. Such calculations appear to be feasible in the near future because of the small number of electrons and few vibrational degrees of freedom. An accurate knowledge of the  $\text{H}_2\text{O}^+ - \text{He}$  interaction potential may also be useful for modeling the chemistry of astrophysical media as well as for future studies of  $\text{H}_2\text{O}^+$  ions embedded in liquid He droplets. The present work demonstrates that the high sensitivity and selectivity of IR photodissociation spectroscopy and mass spectrometry, in combination with *ab initio* methods, provide powerful tools to study intermolecular forces in weakly bound charged complexes.

## Acknowledgement

This study is part of project No. 20-55285.98 of the Swiss National Science Foundation.

## References

- P. Hobza and R. Zahradnik, *Intermolecular Complexes: The Role of van der Waals Systems in Physical Chemistry and in the Bio-disciplines*, Elsevier, Amsterdam, 1988.
- G. A. Jeffrey and W. Saenger, *Hydrogen Bonding in Biological Systems*, Springer, Berlin, 1991.
- E. J. Bieske and O. Dopfer, *Chem. Rev.*, 2000, **100**, 3963.
- S. A. Nizkorodov, J. P. Maier and E. J. Bieske, *J. Chem. Phys.*, 1995, **103**, 1297.
- O. Dopfer, S. A. Nizkorodov, M. Meuwly, E. J. Bieske and J. P. Maier, *Chem. Phys. Lett.*, 1996, **260**, 545.
- M. Meuwly, S. A. Nizkorodov, J. P. Maier and E. J. Bieske, *J. Chem. Phys.*, 1996, **104**, 3876.
- D. Roth, S. A. Nizkorodov, J. P. Maier and O. Dopfer, *J. Chem. Phys.*, 1998, **109**, 3841.
- O. Dopfer, D. Roth and J. P. Maier, *Chem. Phys. Lett.*, 1999, **310**, 201.
- R. V. Olkhov, S. A. Nizkorodov and O. Dopfer, *J. Chem. Phys.*, 1999, **110**, 9527.
- E. J. Bieske, A. S. Soliva, M. Welker and J. P. Maier, *J. Chem. Phys.*, 1990, **93**, 4477.
- A. Carrington, D. I. Gammie, A. M. Shaw, S. M. Taylor and J. M. Hutson, *Chem. Phys. Lett.*, 1996, **260**, 395.
- O. Dopfer, *J. Phys. Chem. A*, 2000, **104**, 11693.
- O. Dopfer, D. Roth and J. P. Maier, *J. Phys. Chem. A*, 2000, **104**, 11702.
- O. Dopfer, D. Roth and J. P. Maier, *J. Chem. Phys.*, 2001, **114**, 7081.
- G. E. Lopez, *J. Comput. Chem.*, 1995, **16**, 768.
- N. M. Lakin, R. V. Olkhov and O. Dopfer, *Faraday Discuss.*, 2001, **118**, DOI: 10.1039/b010232f.
- R. V. Olkhov and O. Dopfer, *Chem. Phys. Lett.*, 1999, **314**, 215.
- F. Tao, Z. Li and Y. Pan, *Chem. Phys. Lett.*, 1996, **255**, 179.
- W. T. Huntress, *Astrophys. J. Suppl.*, 1977, **33**, 495.
- E. Herbst, *Annu. Rev. Phys. Chem.*, 1995, **46**, 27.
- S. A. Nizkorodov, O. Dopfer, T. Ruchti, M. Meuwly, J. P. Maier and E. J. Bieske, *J. Phys. Chem.*, 1995, **99**, 17118.
- E. J. Bieske, *J. Chem. Soc., Faraday Trans.*, 1995, **91**, 1.
- G. Guelachvili and K. N. Rao, *Handbook of Infrared Standards*, Academic Press, New York, 1993.
- M. J. Frisch, G. W. Trucks, H. B. Schlegel, G. E. Scuseria, M. A. Robb, J. R. Cheeseman, V. G. Zakrzewski, J. A. Montgomery, R. E. Stratman, J. C. Burant, S. Dapprich, J. M. Millam, A. D. Daniels, K. N. Kudin, M. C. Strain, O. Farkas, J. Tomasi, V. Barone, M. Cossi, R. Cammi, B. Menucci, C. Pomelli, C. Adamo, S. Clifford, J. Ochterski, G. A. Petersson, P. Y. Ayala, Q. Cui, K. Morokuma, D. K. Malick, D. Rabuck, K. Raghavachari, J. B. Foresman, J. Cioslowski, J. V. Ortiz, B. B. Stefanov, G. Liu, A. Liashenko, P. Piskorz, I. Komaromi, R. Gomperts, R. L. Martin, D. J. Fox, T. Keith, M. A. Al-Laham, C. Y. Peng, A. Nanayakkara, C. Gonzales, M. Challacombe, P. M. W. Gill, B. G. Johnson, W. Chen, M. W. Wong, J. L. Andres, C. Gonzales, M. Head-Gordon, E. S. Replogle and J. A. Pople, *GAUSSIAN 98, Revision A.5.*, Gaussian Inc., Pittsburgh, PA, 1998.
- Extensible Computational Chemistry Environmental Basis Set Data Base*, Version 10, 1996.
- N. M. Lakin, O. Dopfer, M. Meuwly, B. J. Howard and J. P. Maier, *Mol. Phys.*, 2000, **98**, 63.
- S. F. Boys and F. Bernardi, *Mol. Phys.*, 1970, **19**, 553.
- V. Duijneveldt, in *Molecular Interactions*, ed. S. Scheiner, New York, 1997, p. 81.

- 29 S. G. Lias, J. E. Barmess, J. F. Liebman, J. L. Holmes, R. D. Levin and W. G. Mallard, *J. Phys. Chem. Ref. Data Suppl.*, 1988, **17**, 1.
- 30 T. R. Huet, C. J. Pursell, W. C. Ho, B. M. Dinelli and T. Oka, *J. Chem. Phys.*, 1992, **97**, 5977.
- 31 G. Herzberg, *Molecular Spectra and Molecular Structure. III. Electronic Spectra and Electronic Structure of Polyatomic Molecules*, Krieger, Malabar, FL, 1991.
- 32 J. D. Lewis, T. B. Malloy, Jr., T. H. Chao and J. Laane, *J. Mol. Struct.*, 1972, **12**, 427.
- 33 P. Mürzt, L. R. Zink, K. M. Evenson and J. M. Brown, *J. Chem. Phys.*, 1998, **109**, 9744.
- 34 A. S. Pine and W. J. Lafferty, *J. Chem. Phys.*, 1983, **78**, 2154.
- 35 D. Yaron, K. I. Peterson, D. Zolanz, W. Klemperer, F. J. Lovas and R. D. Suenram, *J. Chem. Phys.*, 1990, **92**, 7095.
- 36 R. E. Bumgarner, S. Suzuki, P. A. Stockman, P. G. Green and G. A. Blake, *Chem. Phys. Lett.*, 1991, **176**, 123.
- 37 M. D. Brookes and A. R. W. McKellar, *J. Chem. Phys.*, 1998, **109**, 5823.
- 38 L. Oudejans and R. E. Miller, *Chem. Phys. Lett.*, 1999, **306**, 214.
- 39 G. Herzberg, *Molecular Spectra and Molecular Structure. II. Infrared and Raman Spectra of Polyatomic Molecules*, Krieger, Malabar, FL, 1991.
- 40 W. T. Raynes, *J. Chem. Phys.*, 1964, **41**, 3020.
- 41 J. Israelachvili, *Intermolecular and Surface Forces*, Academic Press, New York, 1992.
- 42 O. Dopfer, D. Roth, R. V. Olkhov and J. P. Maier, *J. Chem. Phys.*, 1999, **110**, 11911.
- 43 R. J. Le Roy, M. R. Davies and M. E. Lam, *J. Phys. Chem.*, 1991, **95**, 2167.
- 44 R. E. Miller, *Acc. Chem. Res.*, 1990, **23**, 10.
- 45 A. Bagno, *J. Chem. Soc., Faraday Trans.*, 1998, **94**, 2501.
- 46 R. C. Cohen and R. J. Saykally, *J. Chem. Phys.*, 1993, **98**, 6007.
- 47 J. van Wijngaarden and W. Jäger, *Mol. Phys.*, 2000, **98**, 1575.
- 48 E. P. L. Hunter and S. G. Lias, *J. Phys. Chem. Ref. Data*, 1998, **27**, 413.
- 49 O. Dopfer, R. V. Olkhov, D. Roth and J. P. Maier, *Chem. Phys. Lett.*, 1998, **296**, 585.
- 50 S. A. Nizkorodov, D. Roth, R. V. Olkhov, J. P. Maier and O. Dopfer, *Chem. Phys. Lett.*, 1997, **278**, 26.